Click Here for Full Article

Simulating the evolution of soot mixing state with a particle-resolved aerosol model

N. Riemer,[1] M. West,[2] R. A. Zaveri,[3] and R. C. Easter[3]

[1] The mixing state of soot particles in the atmosphere is of crucial importance for assessing their climatic impact, since it governs their chemical reactivity, cloud condensation nuclei activity, and radiative properties. To improve the mixing state representation in models, we present a new approach, the stochastic particle-resolved model PartMC-MOSAIC, which explicitly resolves the composition of individual particles in a given population of different types of aerosol particles. This approach tracks the evolution of the mixing state of particles due to emission, dilution, condensation, and coagulation. To make this direct stochastic particle-based method practical, we implemented a new multiscale stochastic coagulation method. With this method we achieved high computational efficiency for situations when the coagulation kernel is highly nonuniform, as is the case for many realistic applications. PartMC-MOSAIC was applied to an idealized urban plume case representative of a large urban area to simulate the evolution of carbonaceous aerosols of different types due to coagulation and condensation. For this urban plume scenario we quantified the individual processes that contributed to the aging of the aerosol distribution, illustrating the capabilities of our modeling approach. The results showed for the first time the multidimensional structure of particle composition, which is usually lost in sectional or modal aerosol models.

1. Introduction

[2] Soot particles are an important constituent of the atmospheric aerosol, since they participate in tropospheric chemistry [*Saathoff et al.*, 2001] and affect human pulmonary health [*Pope and Dockery*, 1996]. Because of its ability to absorb light [*Horvath and Trier*, 1993], soot is also recognized as an important player in the aerosol radiative forcing of climate at global, regional, and local scales [*Menon et al.*, 2002; *Chung and Seinfeld*, 2005; *Roeckner et al.*, 2006]. The source of soot particles is the incomplete combustion of carbon containing material, which means that except for natural biomass burning, all sources of soot are of anthropogenic origin [*Penner*, 1995]. The dominant removal process is wet deposition [*Ducret and Cachier*, 1992]. Soot particles can be transported over long distances reaching remote regions such as the Arctic [*Clarke and Noone*, 1985; *Hansen and Nazarenko*, 2004].

1.1. Observed Properties of Vehicle Particle Emissions

[3] In this paper we investigated an idealized urban plume scenario in which the primary sources of soot were emissions from gasoline and diesel vehicles. Fresh emissions from diesel and gasoline engines consist of a complex particle mixture with respect to composition and mixing state. The main constituents are elemental carbon and organic carbon [*Medalia and Rivin*, 1982; *Andreae and Gelencsér*, 2006], but the precise mixture depends on the individual source and operating conditions. Volatility measurements by *Kittelson et al.* [2006a] showed that diesel exhaust particles from heavy-duty diesel truck engines consisted of more volatile and less volatile particles. Smaller particles (in the nuclei mode) tended to be more volatile and consisted mainly of heavy hydrocarbons, probably from lubricating oil, whereas carbonaceous, solid agglomerates ("soot" particles) formed a majority of the larger particles (in the accumulation mode). The number concentration in the nuclei mode moreover depended on the amount of sulfur in the fuel, and the size distribution and composition typically also depended on the engine load [*Kittelson et al.*, 2006a; *Burtscher et al.*, 1998]. *Burtscher et al.* [1998] found that at high load, i.e., richer combustion conditions, much less volatile material was present in the diesel exhaust compared to low load. Gasoline emissions generally showed a lower elemental carbon content compared to diesel emissions [*Kleeman et al.*, 2000]. *Kittelson et al.* [2006b] reported a mass fraction of 64% elemental

---

[1]Department of Atmospheric Science, University of Illinois at Urbana-Champaign, Urbana, Illinois, USA.
[2]Department of Mechanical Science and Engineering, University of Illinois at Urbana-Champaign, Urbana, Illinois, USA.
[3]Atmospheric Science and Global Change Division, Pacific Northwest National Laboratory, Richland, Washington, USA.

carbon for cold-cold cycles, and 34% elemental carbon for hot cycles. Apart from elemental and organic carbon, trace concentrations of ionic and metallic species were also found in diesel and gasoline exhaust particles [*Kleeman et al.*, 2000; *Weingartner et al.*, 1997]. While the mass fraction of these species are small, the ionic species influence the initial hygroscopic nature of the particles released to the atmosphere. Metallic species present are of interest as they can catalyze heterogeneous chemical reactions within fog droplets [*Erel et al.*, 1993] and may cause adverse health effects [*Dreher et al.*, 1997].

[4] Results from single particle analysis with an ultrafine aerosol time-of-flight mass spectrometer have recently become available [*Toner et al.*, 2006; *Shields et al.*, 2007]. These studies identified seven different particle classes in the exhaust of heavy-duty diesel vehicles. *Toner et al.* [2006] showed that the top three particle classes comprised 91% of the total particles sampled and consisted of elemental carbon and engine lubricating oil. However the study also showed that the results depended on the driving conditions and on the individual vehicle. While these results provide remarkable insight into the details of particle mixing state of exhaust particles, it is to date still difficult to derive quantitative information on the particle composition. *Spencer and Prather* [2006] undertook a step in this direction by deriving a calibration procedure that makes it possible to determine ratios of organic and elemental carbon in individual particles, but challenges remain in obtaining accurate particle composition information.

1.2. Aging of Soot in Atmospheric Models

[5] From the above measurements of vehicle emissions it is clear that freshly emitted soot particles consist of several species, namely elemental carbon, organic carbon, and trace amounts of ionic and metallic species. *Weingartner et al.* [1997] found that freshly emitted soot particles are in general rather hydrophobic, but their initial hygroscopic properties also depended on the sulfur content of the fuel. Moreover, during their transport in the atmosphere their hygroscopic qualities can change owing to coagulation with soluble aerosols, condensation of secondary organic and inorganic species, and photochemical processes. These processes are usually referred to as aging, and they determine the particle growth in response to ambient relative humidity and the ability to be activated as cloud condensation nuclei. The aging processes also have a profound effect on the aerosol optical properties. For example, soot that is coated with nonabsorbing substances shows greater absorptivity compared to soot that is not coated. This effect on radiative properties has been studied by a number of investigators [e.g., *Chýlek et al.*, 1995; *Jacobson*, 2001; *Riemer et al.*, 2003; *Schnaiter et al.*, 2005; *Bond et al.*, 2006]. Field measurements show that atmospheric soot particles contain other species in varying proportions, and that the hydrophobic portion of the aerosol population decreases significantly as the distance from the sources increases [*Andreae et al.*, 1986; *Levin et al.*, 1996; *Okada and Hitzenberger*, 2001; *Johnson et al.*, 2005; *Cubison et al.*, 2008].

[6] Since it is well recognized that soot particles contribute to both the direct and indirect/semidirect climate effect [*Lesins et al.*, 2002; *Jacobson*, 2000, 2002b; *Nenes et al.*, 2002], an adequate representation of soot and its mixing state is sought for use in both global and regional models, and the parameterization of soot aging is key to determining its atmospheric abundance. Many global models have simulated both (fresh) hydrophobic soot and (aged) hydrophilic soot, which can be considered as a minimal representation of the soot mixing state. Several of the models have assumed that the conversion from hydrophobic to hydrophilic soot can be treated as an exponential decay process, with a half-life of approximately 24 h [*Cooke et al.*, 1999; *Lohmann et al.*, 1999; *Koch*, 2001; *Chung and Seinfeld*, 2002]. This approach is a substantial simplification since the conversion rate depends on many different environmental conditions. This has led to more mechanistic approaches, where processes such as condensation of sulfate on soot particles, chemical oxidation and/or coagulation between different particle classes are explicitly modeled to some extent [*Wilson et al.*, 2001; *Stier et al.*, 2005; *Tsigaridis and Kanakidou*, 2003]. *Koch* [2001] and *Croft et al.* [2005] compared different aging parameterizations in global models and concluded that the model results critically depend on the respective formulation.

[7] To better understand the soot aging process it is desirable to have models that are capable of representing the aerosol mixing state. From a computational standpoint, if the aerosol mixing state can be defined in terms of A classes of chemical components (e.g., $A = 8$ with sulfate, nitrate, ammonium, sea salt, hydrophobic organics, soluble organics, black carbon, and mineral dust classes), then the mixing state is an A-dimensional space and the size-resolved particle composition distribution is a multivariate function.

[8] Most existing aerosol models, however, represent the particle population only as a bulk, or as a univariate function of a single independent variable, typically total particle mass, diameter, or similar. To do this it is generally assumed that each particle consists only of a single species (fully externally mixed), or that all particles in the same mode or size bin have identical chemical composition (fully internally mixed). Within this framework the standard methods are sectional, modal, and moment models. Sectional models [e.g., *Wexler et al.*, 1994; *Jacobson*, 1997; *Adams et al.*, 1999; *Zaveri et al.*, 2008] place a grid on the independent variable space and store the number distribution or mass distribution (or both) in each grid cell. Modal models [e.g., *Whitby et al.*, 1991; *Whitby and McMurry*, 1997; *Wilson et al.*, 2001; *Stier et al.*, 2005; *Binkowski and Shankar*, 1995] represent the particle distribution as a sum of modes, each having a lognormal (or similar) size distribution described by a small number of parameters (typically number, mass, and width). Moment models [e.g., *McGraw*, 1997] do not explicitly resolve the distribution, but rather track a few low-order moments of it.

[9] It is possible to extend the standard aerosol models to handle multivariate distributions, for example a two-dimensional distribution that is a function of two species, or a function of volume and area. Such extensions have been investigated for sectional models [*Fassi-Fihri et al.*, 1997], modal models [*Brock et al.*, 1988], and moment models [*Yoon and McGraw*, 2004a, 2004b]. All such models, however, require storage and computation that scale exponentially in the number of independent variables A. For

the model we develop here with $A = 20$ species, fully resolved multivariate sectional, modal, or moment models are infeasibly expensive. For example, a sectional model normally uses on the order of 8–20 size bins to adequately resolve a univariate aerosol distribution, and even then will suffer from numerical diffusion [*Dhaniyala and Wexler*, 1996; *Wu and Biswas*, 1998]. An A-dimensional distribution would thus require 8^A–20^A bins, which is infeasible unless A is much smaller than our 20 species. In contrast, the particle-resolved methods developed in this paper scale with the number of particles, not the dimension of the space they are in.

[10] While traditional univariate aerosol models are too expensive if extended to resolve multivariate aerosol mixing states with more than a few dimensions, there have been a number of extensions proposed to resolve the mixing state to some extent. One example of methods that somewhat resolve the mixing state are the so-called source oriented models developed by *Eldering and Cass* [1996], *Kleeman et al.* [1997], and *Kleeman and Cass* [1998] for regional-scale modeling. In these models, the particles of different sources remain in separate populations and a number of individual size distributions (usually about ten) are tracked, while their mixing states change owing to condensation of secondary substances. However, because the main focus of their studies was the prediction of particle mass distributions, the changes in number concentrations and particle mixing states due to self-coagulation and heterocoagulation of particles from different sources was ignored. Coagulation between aerosol particles is important if one is interested in predicting the number distribution, especially under polluted conditions or if long residence times are considered [*Zhang and Wexler*, 2002]. Nevertheless, the source-oriented approach allows the attribution of pollutants to specific sources and is useful for designing emission control strategies [*Kleeman and Cass*, 1998; *Kleeman et al.*, 1999]. It was used in the framework of a Lagrangian trajectory model, compared to measurements by *Bhave et al.* [2002], and has been extended to a 3D Eulerian model [*Kleeman et al.*, 2001; *Ying et al.*, 2004; *Ying and Kleeman*, 2006]. The Lagrangian version described by *Kleeman and Cass* [1998] treated the mixing state to some extent, with fresh emissions introduced as new size distributions at every hour along the trajectory.

[11] Another variant of mixing state modeling was presented by *Jacobson* [2002a], where a total of 18 interacting aerosol size distributions were considered. His approach was not source oriented to the degree of *Kleeman et al.* [2001], since anthropogenic emissions from specific sectors were not resolved, but primary mineral dust, sea salt, organic matter, and black carbon were treated. Three distributions represented particles containing different proportions of black carbon. Coagulation between different particle classes was included, and 11 of the 18 particle classes were used to represent the mixed particles that arise owing to coagulation interaction of two primary species. Interactions that would result in the formation of a particle with three different constituents resulted in a "mixed" particle and were not tracked further. Despite this considerable complexity the limitation remained that particles for a certain particle class and size were considered to have identical compositions, and the emissions into the primary particle categories were instantly aged.

[12] *Riemer et al.* [2003] presented an approach for mixing state modeling of soot using a mesoscale modal modeling framework. Five modes described the composition and size distribution of submicron particles, consisting of one pure-soot mode, two soot-free modes (with particles containing a mixture of inorganic and organic species), and two soot-containing modes (with particles containing a mixture of soot, inorganics and organics). The last two modes thus represented aged soot particles, and aging occurred either by coagulation between modes or by condensation of secondary substances. While this treatment allowed the distinction between fresh and aged soot, the simplifying assumption was made that within each mode all particles had identical compositions.

1.3. Particle-Resolved Models for Representing Mixing State

[13] Here we present a particle-resolved model, PartMC, that explicitly stores the composition of many individual aerosol particles (about 10^5) within a well-mixed computational volume. Relative particle positions within this computational volume are not tracked, but rather the coagulation process is simulated stochastically by assuming that coagulation events are Poisson distributed with a Brownian kernel.

[14] Applying such a Monte Carlo approach for simulating the evolution of particle distributions dates back to *Gillespie* [1975], who developed the exact Stochastic Simulation Algorithm [see also *Gillespie*, 1976, 1977, 1992] to treat the stochastic collision-coalescence process in clouds. Variants of Gillespie's algorithm are widely used in different fields, including simulations of gene regulatory networks [*El Samad et al.*, 2005], chemical kinetics [*Gillespie*, 2007], and sintering in flames [*Wells et al.*, 2006].

[15] Since *Gillespie* [1975], particle-resolved methods have been used to study aerosols by many authors. We do not attempt to give a comprehensive literature survey here. *Babovsky* [1999] and *Eibeck and Wagner* [2001] developed the Mass Flow Algorithm with variable computational/ physical particle ratios, *Kolodko and Sabelfeld* [2003] gave relevant error estimates, and *Debry et al.* [2003] coupled it to evaporation and condensation. Somewhat similarly, *Laurenzi et al.* [2002] and *Alfonso et al.* [2008] (on the basis of ideas from *Spouge* [1985]) stored the number of particles with identical composition to reduce memory usage and computational expense while using Gillespie's method. *Guias* [1997] studied convergence of stochastic coagulation to the Smolukowski equation. *Efendiev and Zachariah* [2002] investigated enclosures within aerosols using a particle-based method, while *Maisels et al.* [2004] used particle methods with simultaneous nucleation, coagulation, and surface growth.

[16] While not focused on aerosol simulations, much recent work has investigated efficient simulation methods for reaction-type Markov processes. *Gillespie* [2001] developed the tau-leaping method for efficient generation of many events with near-constant rates, with extensions by *Gillespie and Petzold* [2003], *Rathinam et al.* [2003], *Cao et al.* [2006] and others, including for multiscale systems with scale separation by *Cao et al.* [2005]. Multiscale

variants of Gillespie's Stochastic Simulation Algorithm have also been developed by *E et al.* [2007]. *Gibson and Bruck* [2000] developed the Next Reaction Method for efficient exact sampling, which stores and reuses event calculations for efficiency. *Anderson* [2007, 2008] developed efficient simulation algorithms based on the Next Reaction Method and the tau-leaping method.

[17] For the large number of particles in the simulations in this paper, we used an efficient approximate coagulation method, as described in section 4. This used a binned sampling method to efficiently sample from the highly multiscale coagulation kernel in the presence of a very nonuniform particle size distribution, implemented with a multievent-per-time-step sampling of the coagulation events. Multirate versions of Gillespie's method have been developed previously by *Cao et al.* [2005] and *E et al.* [2007], but relied on scale separation to average slow event rates over fast timescales. The method used here does not accelerate rare events but it does accelerate the generation of events without scale separation, as needed for the smoothly varying coagulation kernels and particle size distributions. The PartMC coagulation method has storage cost proportional to the number of physical particles, computational cost for evaporation/condensation proportional to the number of particles, and computational cost for coagulation proportional to the number of coagulation events.

[18] PartMC was coupled with the new state-of-the-art aerosol chemistry model MOSAIC [*Zaveri et al.*, 2008], which simulates the gas and particle phase chemistries, particle phase thermodynamics, and dynamic gas-particle mass transfer in a deterministic manner. The coupled model system, PartMC-MOSAIC, predicts number, mass, and full composition distributions, and is therefore suited for applications where any or all of these quantities are required.

[19] Simulating all particles explicitly in a population of aerosol completely eliminates any errors associated with numerical diffusion. As a result, the treatment of aerosol mixing state dynamics and chemistry makes PartMC-MOSAIC suitable for use as a numerical benchmark of mixing state for more approximate models, as has been shown already by *McGraw et al.* [2008]. It can also be applied to different environments going beyond the example of clear-sky photochemistry shown in this paper, including the in-cloud processing of aerosol, and it can be used to accurately estimate quantities that depend on the mixing state, such as cloud condensation nuclei spectra and optical properties, which we will address in a forthcoming paper. The current version of PartMC is available under the GNU General Public License (GPL) at http://lagrange.mechse. illinois.edu/mwest/partmc/, and the MOSAIC code is available upon request from R. A. Zaveri.

[20] The main contributions of this paper are: (1) an accelerated stochastic coagulation method for multiscale kernels, (2) the coupling of a particle resolved model with a gas- and aerosol-chemistry code, and (3) an initial study of the soot mixing states present in a typical polluted urban environment. This manuscript is organized as follows. In section 2 we write the governing equations for the coupled gas-aerosol box model and discuss the approximations needed by this model of the physical system. The numerical approximation to the governing equations is given in section 3, where we introduce the particle-resolved aerosol model PartMC and describe how it is coupled to the gas- and aerosol-chemistry code MOSAIC. In section 4 we give the efficient coagulation algorithm used by PartMC and verify its performance numerically. Finally, section 5 focuses on the evolution of the mixing state of soot particles in an idealized urban plume scenario. The primary value of the study in section 5 is to demonstrate the new model capabilities. It also begins to address the question of what experimental data would be helpful in studying the effects of aerosol particle composition, and what the effects are of ignoring mixing state in existing models.

2. Coupled Aerosol-Gas Governing Equations

[21] We consider a Lagrangian parcel framework where we simulate the evolution of aerosol particles and trace gases in single parcel (or volume) of air moving along a specified trajectory. In addition to coagulation and aerosol and gas chemistry, the model treats prescribed emissions of aerosols and gases, and mixing of the parcel with background air. Within the air parcel we do not track the physical location of aerosol particles and we assume homogeneous environmental conditions and gas concentrations.

[22] An aerosol particle contains mass $\mu_a \geq 0$ (kg) of species a, for $a = 1,\ldots,A$, so that the particle composition is described by the A-dimensional vector $\vec{\mu} \in \mathbb{R}^A$. The quantity μ_{all} (kg) is the total wet mass of the particle, and $\mu_{\mathrm{dry}} = \mu_{\mathrm{all}} - \mu_{\mathrm{H_2O}}$ (kg) is the total dry mass. The cumulative aerosol number distribution at time t and constituent masses $\vec{\mu} \in \mathbb{R}^A$ is $N(\vec{\mu}, t)$ (m^{-3}), which is defined to be the number concentration of aerosol particles that contain less than μ_a mass of species a, for all $a = 1,\ldots,A$. The aerosol number distribution at time t and constituent masses $\vec{\mu} \in \mathbb{R}^A$ is $n(\vec{\mu}, t)$ (m^{-3} kg^{-A}), which is defined by

$$n(\vec{\mu}, t) = \frac{\partial^A N(\vec{\mu}, t)}{\partial \mu_1 \partial \mu_2 \ldots \partial \mu_A}. \tag{1}$$

[23] The concentration of trace gas phase species i at time t is given by $g_i(t)$ (mol m^{-3}), for $i = 1,\ldots,G$, so the trace gas phase species concentrations are the G-dimensional vector $\vec{g}(t) \in \mathbb{R}^G$. We assume that the aerosol and gas species are numbered so that the first C species of each undergo gas to particle conversion, and that they are in the same order so that gas species i converts to aerosol species i, for $i = 1,\ldots,C$. We further assume that aerosol species $C + 1$ is water.

[24] The environment is described by temperature $T(t)$ (K), pressure $p(t)$ (Pa), relative humidity RH(t) (dimensionless), and dry air density $\rho_{\mathrm{dry}}(t)$ (kg m^{-3}). For the simulation in section 5 the air temperature is prescribed as a function of time, while the air pressure and water mixing ratio are kept constant and the relative humidity and dry air density are updated accordingly.

[25] We assume that we are modeling a vertical slice of a well-mixed boundary layer during the day and a slice of the residual layer during the night, always surrounded to the sides and above by background air that contains prescribed background gas and aerosol. The height of the boundary layer is given by $H(t)$ (m). We denote by $\lambda_{\mathrm{dil,horiz}}(t)$ (s^{-1}) the horizontal dilution rate with the prescribed background gas and aerosol, and by $\lambda_{\mathrm{dil,vert}}(t)$ (s^{-1}) the vertical dilution rate

that represents entrainment of a growing boundary layer. The total dilution rate $\lambda_{\text{dil}}(t)$ (s^{-1}) is then given by

$$\lambda_{\text{dil}}(t) = \lambda_{\text{dil,horiz}}(t) + \lambda_{\text{dil,vert}}(t) \tag{2}$$

$$\lambda_{\text{dil,vert}} = I_{\text{entrain}}(t) \max\left(0, \frac{1}{H(t)}\frac{dH(t)}{dt}\right), \tag{3}$$

where vertical entrainment only occurs for increasing boundary layer heights. The indicator $I_{\text{entrain}}(t)$ is 1 when the modeled air parcel is within the boundary layer and so entrainment is possible, and is 0 when the air parcel is in the residual layer.

[26] The mean evolution of the stochastic particle coagulation process in the limit of a large number of particles, neglecting fluctuation correlations between the number of particles of different sizes [*Gillespie*, 1972], is the classical Smoluchowski coagulation equation [*von Smoluchowski*, 1916a, 1916b], which for a multidimensional aerosol distribution with gas coupling is given in equations (4) and (5),

Many of the rates, coefficients and functions also depend on the environmental conditions, but we have not written this dependence explicitly.

3. Particle-Resolved Aerosol Models

3.1. PartMC Aerosol State Representation

[27] We consider a Lagrangian parcel with volume V (m^3), also called the computational volume. We represent the aerosol state by storing N_p particles in this volume, written $\Pi = (\vec{\mu}^1, \vec{\mu}^2, \ldots, \vec{\mu}^{N_p})$, where the particle order is not significant. Each particle is an A-dimensional vector $\vec{\mu}^i \in \mathbb{R}^A$ with components $(\mu_1^i, \mu_2^i, \ldots, \mu_A^i)$, so μ_a^i is the mass of species a in particle i, for $a = 1, \ldots, A$ and $i = 1, \ldots, N_p$. In the notation of *Debry et al.* [2003] for the Mass Flow Algorithm, we are taking $(\omega_i/y_i)(t) = 1$, which means one computational particle per physical particle. While we track every particle within the computational volume V, we regard this volume as being representative of a much larger air parcel. For example, in section 5 we use a computational volume on the order of a few cubic centimeters but take this

$$\frac{\partial n(\vec{\mu}, t)}{\partial t} = \underbrace{\frac{1}{2} \int_0^{\mu_1} \int_0^{\mu_2} \cdots \int_0^{\mu_A} K(\vec{\mu}', \vec{\mu} - \vec{\mu}') n(\vec{\mu}', t) n(\vec{\mu} - \vec{\mu}', t) d\mu_1' d\mu_2' \ldots d\mu_A'}_{\text{coagulation gain}}$$

$$\underbrace{- \int_0^\infty \int_0^\infty \cdots \int_0^\infty K(\vec{\mu}, \vec{\mu}') n(\vec{\mu}, t) n(\vec{\mu}', t) d\mu_1' d\mu_2' \ldots d\mu_A'}_{\text{coagulation loss}} + \underbrace{\dot{n}_{\text{emit}}(\vec{\mu}, t)}_{\text{emission}} + \underbrace{\lambda_{\text{dil}}(t)(n_{\text{back}}(\vec{\mu}, t) - n(\vec{\mu}, t))}_{\text{dilution}}$$

$$\underbrace{- \sum_{i=1}^C \frac{\partial}{\partial \mu_i}(c_i I_i(\vec{\mu}, \vec{g}, t) n(\vec{\mu}, t))}_{\text{gas-particle transfer}} - \underbrace{\frac{\partial}{\partial \mu_{C+1}}(c_w I_w(\vec{\mu}, \vec{g}, t) n(\vec{\mu}, t))}_{\text{water transfer}} + \underbrace{\frac{1}{\rho_{\text{dry}}(t)}\frac{d\rho_{\text{dry}}(t)}{dt} n(\vec{\mu}, t)}_{\text{air density change}} \tag{4}$$

$$\frac{dg_i(t)}{dt} = \underbrace{\dot{g}_{\text{emit},i}(t)}_{\text{emission}} + \underbrace{\lambda_{\text{dil}}(t)\left(g_{\text{back},i}(t) - g_i(t)\right)}_{\text{dilution}} + \underbrace{R_i(\vec{g})}_{\text{chemical reactions}} + \underbrace{\frac{1}{\rho_{\text{dry}}(t)}\frac{d\rho_{\text{dry}}(t)}{dt} g_i(t)}_{\text{air density change}}$$

$$\underbrace{- \int_0^\infty \int_0^\infty \cdots \int_0^\infty I_i(\vec{\mu}, \vec{g}, t) n(\vec{\mu}, t) d\mu_1 d\mu_2 \ldots d\mu_A}_{\text{gas-particle transfer}}. \tag{5}$$

The integrodifferential equations (4) and (5) must be augmented with appropriate boundary conditions, which are chosen on physical grounds to ensure that the constituent masses of particles cannot become negative and mass is conserved. In equation (4), $K(\vec{\mu}_1, \vec{\mu}_2)$ $(m^3\ s^{-1})$ is the coagulation rate between particles with constituent masses $\vec{\mu}_1$ and $\vec{\mu}_2$, $\dot{n}_{\text{emit}}(\vec{\mu}, t)$ $(m^{-3}\ kg^{-A}\ s^{-1})$ is the number distribution rate of aerosol emissions, $n_{\text{back}}(\vec{\mu}, t)$ $(m^{-3}\ kg^{-A})$ is the background number distribution, $I_i(\vec{\mu}, \vec{g}, t)$ $(mol\ s^{-1})$ is the condensation flux of gas species i (with $I_w(\vec{\mu}, \vec{g}, t)$ the flux for water), c_i $(kg\ mol^{-1})$ is the conversion factor from moles of gas species i to mass of aerosol species i (with c_w the factor for water). In equation (5), $\dot{g}_{\text{emit},i}(t)$ $(mol\ m^{-3}\ s^{-1})$ is the emission rate of gas species i, $g_{\text{back},i}(t)$ $(mol\ m^{-3})$ is the background concentration of gas species i, and $R_i(\vec{g})$ $(mol\ m^{-3}\ s^{-1})$ is the concentration growth rate of gas species i due to gas chemical reactions.

to be approximating the state of the well-mixed boundary layer during the day and the residual layer during the night.

[28] The simulation of the aerosol state proceeds by two mechanisms. First, the composition of each particle can change, changing the components of the vector $\vec{\mu}^i$ as species condense from the gas phase and evaporate to it, for example. Second, the population Π can have particles added and removed, either by emissions, dilution or coagulation events between particles.

[29] The representation of the aerosol as a finite collection of particles Π in a volume V is very flexible, as other properties can easily be stored for each particle, such as fractal dimension, electric charge, age since emission, etc. In the present paper we store the number of coagulation events undergone by each particle to produce Figure 15 in section 5.6.

3.2. PartMC Emissions

[30] Because we are using a finite number of particles to approximate the current aerosol population, we need to add a finite number of emitted particles to the volume at each time step. Over time these finite particle samplings should approximate the continuum emission distribution, so the samplings at each time step must be different. We assume that emissions are memoryless, so that emission of each particle is uncorrelated with emission of any other particle. Under this assumption the appropriate statistics are Poisson distributed, whereby the distribution of finite particles is parameterized by the mean emission rate and distribution.

[31] Consider an emission rate $\dot{n}_{\text{emit}}(\vec{\mu}, t)$ $(\text{m}^{-3}\,\text{kg}^{-A}\,\text{s}^{-1})$ of particles as in the emission term of equation (4), a volume V (m^3), and a time step Δt (s). The emissions over the time step from time t_0 to $t_1 = t_0 + \Delta t$ are given by

$$n_{\text{emit}}(\vec{\mu}; t_0, t_1) = \int_{t_0}^{t_1} \dot{n}_{\text{emit}}(\vec{\mu}, t)\, dt \qquad (6)$$

$$\approx (t_1 - t_0)\dot{n}_{\text{emit}}(\vec{\mu}, t_0), \qquad (7)$$

for which we use the first-order approximation above. To obtain a finite Poisson sample of the number distribution $n(\vec{\mu}) = n_{\text{emit}}(\vec{\mu}; t_0, t_1)$ $(\text{m}^{-3}\,\text{kg}^{-A})$ in the computational volume V we first see that the mean number $N(n,V)$ of sampled particles will be

$$N_{\text{mean}}(n, V) = \int_0^\infty \int_0^\infty \cdots \int_0^\infty n(\vec{\mu}) V\, d\mu_1\, d\mu_2 \ldots d\mu_A. \quad (8)$$

The actual number S of emitted particles added in a time step will be Poisson distributed, written $S \sim \text{Pois}(\lambda)$, for mean $\lambda = N_{\text{mean}}(n,V)$, so that

$$\text{Prob}(S = k) = \frac{\lambda^k e^{-\lambda}}{k!} \text{ for } k \in \mathbb{Z}^+. \qquad (9)$$

A Poisson sampling Π_{samp} of the number distribution $n(\vec{\mu})$ in volume V, written $\Pi_{\text{samp}} \sim \text{Pois}_{\text{dist}}(n,V)$, is a finite sequence of particles given by

$$\Pi_{\text{samp}} = (\vec{\mu}^1, \vec{\mu}^2, \ldots, \vec{\mu}^S), \qquad (10a)$$

$$S \sim \text{Pois}(N_{\text{mean}}(n, V)), \qquad (10b)$$

$$\vec{\mu}^s \sim \frac{n(\vec{\mu})V}{N_{\text{mean}}(n, V)} \text{ for } s = 1, \ldots, S, \qquad (10c)$$

where (10c) means that each particle has a composition drawn from the distribution specified by $n(\vec{\mu})$.

3.3. PartMC Dilution

[32] As with emissions, we must also obtain a finite sampling of background particles that have diluted into our computational volume during each time step. In addition, some of the particles in our current sample will dilute out of our volume and will be lost, so this must be sampled as well. We assume that dilution is memoryless, so that dilution of each particle is uncorrelated with the dilution of

any other particle or itself at other times, and that once a particle dilutes out it is lost.

[33] Let the background particle distribution be $n_{\text{back}}(\vec{\mu}, t)$ $(\text{m}^{-3}\,\text{kg}^{-A})$, the computational volume be V (m^3), and the time step be Δt (s). The distribution of particles that dilute from the background into the volume V between times t_0 and $t_1 = t_0 + \Delta t$ is $n_{\text{dil}}(\vec{\mu}; t_0, t_1)$, where $n_{\text{dil}}(\vec{\mu}; t_0, t)$ satisfies

$$\frac{\partial n_{\text{dil}}(\vec{\mu}; t_0, t)}{\partial t} = \lambda_{\text{dil}}(t)(n_{\text{back}}(\vec{\mu}, t) - n_{\text{dil}}(\vec{\mu}; t_0, t)) \qquad (11a)$$

$$n_{\text{dil}}(\vec{\mu}; t_0, t_0) = 0. \qquad (11b)$$

[34] We use the first-order approximation given by

$$n_{\text{dil}}(\vec{\mu}; t_0, t_1) \approx (t_1 - t_0)\lambda_{\text{dil}}(t_0)n_{\text{back}}(\vec{\mu}, t_0). \qquad (12)$$

A discrete sampling of $n_{\text{dil}}(\vec{\mu}; t_0, t_1)$ is then given by $\Pi_{\text{dil}} \sim \text{Pois}_{\text{dist}}(n_{\text{dil}}(\vec{\mu}), V)$, as in (10).

[35] If we start the time step at time t_0 with the particle population Π, then each particle in Π has probability $p(t_0, t_1)$ to be lost by dilution during the time step, where $p(t_0, t)$ satisfies

$$\frac{\partial p(t_0, t)}{\partial t} = \lambda_{\text{dil}}(t)(1 - p(t_0, t)) \qquad (13a)$$

$$p(t_0, t_0) = 0. \qquad (13b)$$

We use the first-order approximation given by

$$p(t_0, t_1) \approx (t_1 - t_0)\lambda_{\text{dil}}(t_0). \qquad (14)$$

We denote the binomial distribution for number n and probability p by $B(n, p)$. The number of particles lost from Π between times t_0 and $t_1 = t_0 + \Delta t$ is then given by N_{loss}, which is distributed as

$$N_{\text{loss}} \sim B(N_p, p(t_0, t_1)) \approx \text{Pois}(N_p p(t_0, t_1)). \qquad (15)$$

We approximate the binomial distribution with a Poisson distribution as above, which converges as $\Delta t \to 0$ for fixed N_p. As each particle has equal probability to be lost owing to dilution, we can sample N_{loss} and then choose N_{loss} particles uniformly from Π to be removed.

3.4. Coupled PartMC-MOSAIC Method

[36] We coupled the stochastic PartMC particle-resolved aerosol model to the deterministic MOSAIC gas- and aerosol-chemistry code in a time- or operator-splitting fashion [Press et al., 2007, section 20.3.3] to obtain a complete discretization of the governing equations (4) and (5). The aerosol distribution $n(\vec{\mu}, t)$ is represented by N_p particles in a computational volume V, as described above, while the gas vector $\vec{g}(t)$ stores the gas concentrations. The terms for aerosol coagulation, emissions and dilution are solved stochastically by the PartMC code. The terms for gas chemical reactions, emissions and dilution in equation (5) are integrated deterministically by the MOSAIC code, as are

the gas-particle transfer terms in equations (4) and (5). The terms that represent air density changes are implemented deterministically by scaling $\vec{g}$ and V by the proportional change in dry air density or its inverse, respectively. The full coupled PartMC-MOSAIC algorithm is given here.

Π is the sequence of particle compositions
V is the computational volume
$\vec{g}$ is the gas concentrations
$t = 0$
while $t < t_{\text{final}}$ do:
　$t = t + \Delta t$
　update temperature $T(t)$, pressure $p(t)$, relative humidity
　　$RH(t)$, dry air density $\rho_{\text{dry}}(t)$, and mixing height $H(t)$

$$V(t) = V(t - \Delta t) \frac{\rho_{\text{dry}}(t - \Delta t)}{\rho_{\text{dry}}(t)}$$

$$\vec{g}(t) = \vec{g}(t - \Delta t) \frac{\rho_{\text{dry}}(t)}{\rho_{\text{dry}}(t - \Delta t)}$$

　perform one Δt-time step of coagulation for Π with the
　　PartMC algorithm given in section 4.3
　add $\Delta t\, \dot{\vec{g}}_{\text{emit}}(t) + \Delta t\, \lambda_{\text{dil}}(t)\, (\vec{g}_{\text{back}}(t) - \vec{g}(t))$ to $\vec{g}$
　randomly choose $N_{\text{loss}} \sim \text{Pois}(\Delta t\, \lambda_{\text{dil}} N_{\text{p}})$ and remove
　　N_{loss} randomly chosen particles from Π
　add a sample of $\text{Pois}_{\text{dist}}(\lambda_{\text{dil}}\, \Delta t\, n_{\text{back}}(\cdot, t), V)$ to Π
　add a sample of $\text{Pois}_{\text{dist}}(\Delta t\, \dot{n}_{\text{emit}}(\cdot, t), V)$ to Π
　integrate with MOSAIC for time Δt the system of
　　coupled ODEs given by the gas-particle transfer terms
　　and chemical reactions term from equations (4) and (5)
　output data for time t
end while

[37] The current version of MOSAIC treats all the locally and globally important aerosol species including SO_4, NO_3, Cl, CO_3, MSA (methanesulfonic acid), NH_4, Na, Ca, other inorganic mass (which includes species such as SiO_2, metal oxides, and other unmeasured or unknown inorganic species present in aerosols), black carbon (BC), primary organic aerosol (POA), and secondary organic aerosol (SOA). It consists of four computationally efficient modules: (1) the gas phase photochemical mechanism CBM-Z [*Zaveri and Peters*, 1999]; (2) the Multicomponent Taylor Expansion Method (MTEM) for estimating activity coefficients of electrolytes and ions in aqueous solutions [*Zaveri et al.*, 2005b]; (3) the Multicomponent Equilibrium Solver for Aerosols (MESA) for intraparticle solid-liquid partitioning [*Zaveri et al.*, 2005a]; and (4) the Adaptive Step Time-split Euler Method (ASTEM) for dynamic gas-particle partitioning over size- and composition-resolved aerosol [*Zaveri et al.*, 2008]. The version of MOSAIC box model implemented here also includes a treatment for SOA based on the SORGAM scheme [*Schell et al.*, 2001].

4. PartMC Coagulation Algorithm
4.1. Stochastic Coagulation Simulation

[38] For a population of N_{p} particles there are $N_{\text{p}}(N_{\text{p}} - 1)/2$ possible coagulation events, with the probability rate of a coagulation between particles i and j in a volume V given by $K(\vec{\mu}^i, \vec{\mu}^j)/V$ for the coagulation kernel $K(\vec{\mu}^i, \vec{\mu}^j)$ ($\text{m}^3\,\text{s}^{-1}$). A stochastic coagulation simulation generates a sequence

of coagulation events, each consisting of a pair of particles (i, j) that coagulate and a time Δt until the coagulation occurs. For each coagulation event, the particles i and j are removed from the population Π, a new particle is added to Π with composition $\vec{\mu}^{\text{new}} = \vec{\mu}^i + \vec{\mu}^j$, and the time is advanced by Δt. A new coagulation event is then generated and the process repeated.

[39] The standard stochastic simulation algorithm for coagulation and similar processes is from *Gillespie* [1975] and is based on the observation that the probability density for the time until the next coagulation event is

$$P(\Delta t) = \frac{K_{\text{tot}}}{V} e^{-K_{\text{tot}} \Delta t / V}, \tag{16}$$

where $K_{\text{tot}} = \sum_{i<j} K(\vec{\mu}^i, \vec{\mu}^j)$ is the total rate. We can thus generate an elapsed time by sampling the probability density function (16). The conditional probability that the coagulation event that occurred was between particles i and j is then

$$P(i, j \mid \Delta t) = \frac{K(\vec{\mu}^i, \vec{\mu}^j)}{K_{\text{tot}}}, \tag{17}$$

and this can be sampled to determine which particles coagulated, and then the coagulation event can be performed.

[40] Gillespie's method has the advantage that it generates exact realizations of the stochastic coagulation process. It faces two main difficulties in practice, however. First, the total rate K_{tot} continually changes as coagulation events occur and particle compositions change owing to condensation. Computing a reasonable estimate of this parameter quickly becomes exceedingly expensive, and approximations made to speed up this estimate introduce errors that are difficult to estimate and control. Second, while sampling (16) is very cheap, sampling (17) can be expensive for complex kernels. The two main methods are use of the cumulative distribution function, which scales badly in the number of particles and is thus too expensive for large particle numbers, and use of accept-reject. While accept-reject scales well as the number of particles grows, it is very inefficient if the kernel K is highly nonuniform, as is unfortunately the case for many physically relevant aerosol distributions. Despite these difficulties, Gillespie's method is by far the most commonly used method in practice, with many slight variants appearing in the literature [e.g., see *Efendiev and Zachariah*, 2002; *Kruis et al.*, 2000; *Garcia et al.*, 1987; *Fichthorn and Weinberg*, 1991].

[41] To avoid these two difficulties we formulate an improved method. We use a fixed time step method and we develop a binned acceptance procedure. The use of a fixed time step removes the need to know K_{tot}, albeit with the introduction of some error. This fixed time step also makes it easy to integrate the coagulation with other physics and chemistry using a time-splitting scheme. The binned sampling method means that we are not subject to slowdowns from nonuniform kernels.

4.2. Fixed Time Step Stochastic Coagulation

[42] We choose a fixed time step Δt and in each time step choose N_{test} particle pairs to test. We then generate N_{test}

random particle pairs uniformly and for each pair (i, j) we accept a coagulation event with probability

$$P(i,j) = \frac{K(\vec{\mu}^i, \vec{\mu}^j)\Delta t}{V}\frac{N_p(N_p - 1)}{N_{test}}. \quad (18)$$

In the limit $\Delta t \to 0$ this generates an exact realization of the stochastic coagulation process, and for finite Δt introduces a discretization error. The number N_{test} should be chosen large enough that $P(i,j) \leq 1$ for all pairs (i,j) and for convergence it must remain bounded away from zero as $\Delta t \to 0$. This is similar to the sampling technique used by *Debry et al.* [2003].

[43]   The efficiency of the method, as with any procedure of accept-reject type, is greatest when the maximum value of $P(i, j)$ is as close as possible to 1. To ensure this we choose

$$N_{test} = \lceil K_{max} \Delta t N_p (N_p - 1)/V \rceil, \quad (19)$$

where $K_{max} = \max_{i,j} K(\vec{\mu}^i, \vec{\mu}^j)$ is the maximum kernel value and $\lceil x \rceil$ is the least integer greater than or equal to x. In practice we take K_{max} to be a cheaply computable upper bound for $K(\vec{\mu}^i, \vec{\mu}^j)$, which slightly increases the accuracy of the method and is much cheaper. We precompute this upper bound by sampling a range of particle sizes (and particle densities for the Brownian kernel) in each bin, which works for any kernel function.

[44]   The fixed time step method thus cleanly resolves the difficulties with Gillespie's method to do with the need to determine K_{tot}. It still has the problem, however, that if the kernel $K(\vec{\mu}^i, \vec{\mu}^j)$ is very nonuniform then the acceptance procedure will be very inefficient. To fix this, we adopt a binned approach.

4.3. Binned Stochastic Coagulation

[45]   For coagulation kernels of physical interest, such as those arising from Brownian motion or gravitational settling, the kernel $K(\vec{\mu}^i, \vec{\mu}^j)$ is highly multiscale, with many orders of magnitude difference between the highest and lowest rates. This is a problem for the sampling procedure outlined in section 4.2, because N_{test} will be very large and so we will have to reject many events for each accepted event.

[46]   To accelerate this procedure we take advantage of the fact that the kernel $K(\vec{\mu}^i, \vec{\mu}^j)$ is not random in its nonuniformity, but rather depends primarily on the diameter of the particles. This means that if pairs (i,j) and (k,ℓ) are similar, so that the diameters of particles i and k are close, as are the diameters of particles j and ℓ, then $K(\vec{\mu}^i, \vec{\mu}^j) \approx K(\vec{\mu}^k, \vec{\mu}^\ell)$. We thus group particles into bins sorted by diameter and we use the acceptance procedure (18) for each pair of bins separately. This binned approach ensures that all particle pairs under consideration in a particular iteration have similar coagulation rates, and hence the procedure will have a high proportion of acceptances. Use of a binned version of the fixed time step algorithm means that the number of samples (19) done per pair of bins is automatically adapted to the number of particles in those bins. It also allows us to precompute the K_{max} values for each bin pair. The resulting algorithm is given here.

divide diameter axis into bins as for a sectional model
$N_p(b)$ is the number of particle in bin b

$\vec{\mu}(b, i)$ is the mass vector of the i-th particle in bin b
$K_{max}(b_1, b_2)$ is a precomputed upper bound on the kernel
   for any particles from bins b_1 and b_2
Δt is the timestep
for all bin pairs (b_1, b_2) do:
   $N_{event} = N_p(b_1)N_p(b_2)/2$
   $N_{test} = \lceil K_{max}(b_1, b_2) \Delta t N_{event} /V \rceil$
   for N_{test} repetitions do:
      randomly choose particles i_1 and i_2 uniformly
         in bins b_1 and b_2
      $K_{12} = K(\vec{\mu}(b_1, i_1), \vec{\mu}(b_2, i_2))$
      randomly choose r uniformly in $[0, 1]$
      if $r < K_{12} \Delta t N_{event}/(N_{test}V)$ then:
         coagulate the two particles, updating the
            arrays $N(b)$ and $\vec{\mu}(b, i)$
      end if
   end for
end for

[47]   The primary disadvantage of using a binned sampling procedure is in code complexity, as the bin structures of particles with similar sizes need to be constructed and maintained. This also adds a small amount of computational overhead to the coagulation routine, which is far outweighed by the enormous efficiency gains. We should note that the binned sampling procedure introduces no error in the simulation and is a pure efficiency gain. For typical aerosol profiles the binned procedure gives about $2-4$ orders-of-magnitude speedup in computational time, as quantified in section 4.4.

[48]   The number of particles in the simulation changes over time as particles are added by emissions and dilution and removed by coagulation and dilution. To maintain adequate statistics while avoiding computational limits, we occasionally adjust the particle number. Whenever the number of particles becomes less than half of the original particle number then we double the computational volume and double the number of particles by duplicating each particle. Whenever we have more than twice the original number of particles then we halve the computational volume and discard half of the particles, chosen at random.

[49]   For some kernels, such as the Brownian kernel used in section 5, the kernel is primarily dependent on the particle diameters but also depends on particle density. We could store the particles sorted into a 2D array per diameter bin and per density bin, but the particle density variation is bounded and small enough that it is still reasonably efficient to store them only per diameter bin and to compute K_{max} to take the maximum particle density variation into account.

[50]   To enable efficient coagulation, the particle array Π is stored as an array of pointers to partially filled particle arrays, one per diameter-bin. Insertions into bin arrays are performed at the end of the currently filled area and deletions from the middle are followed by a shift of the last element into the gap, ensuring full packing of each bin array at all times. Each diameter-bin array is reallocated to twice its existing size when necessary or half its existing size when possible. This gives constant-time random access at the cost of $O(\log \Delta N_p)$ reallocations and at most twice the minimal memory usage.
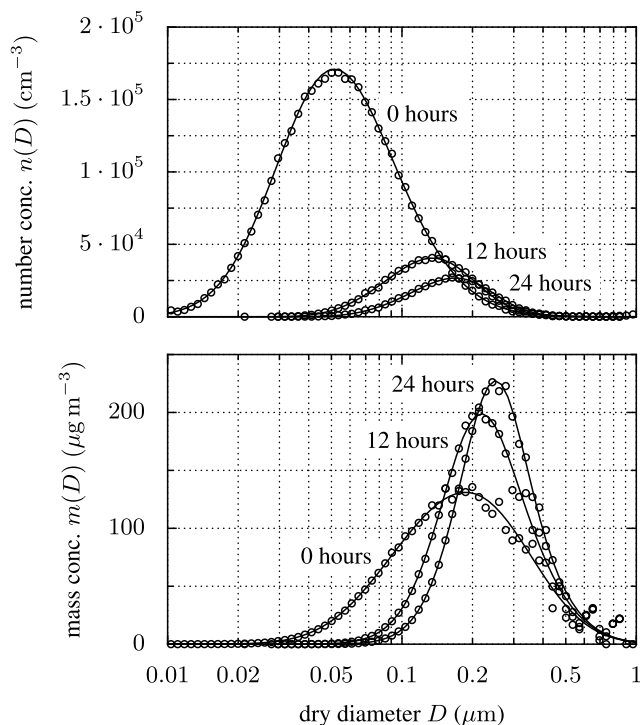
Figure 1. Comparison of the stochastic particle-resolved method using 10^5 particles (circles) against a sectional solution (lines) to the Smoluchowski equation for the Brownian kernel according to *Jacobson* [1999]. The number and mass distributions $n(D)$ and $m(D)$ are defined by equations (20) and (21), respectively.

4.4. Verification of the PartMC Algorithms

[51] For verification of the PartMC stochastic coagulation method we compared PartMC against a sectional solution to the Smoluchowski equation for a Brownian kernel [*Jacobson*, 1999]. For this test we used a single PartMC run with 10^5 particles and a time step of $\Delta t = 1$ min (all identical to the simulation in section 5), while the sectional model was that of *Bott* [1998], using a time step of $\Delta t = 1$ s and 220 logarithmically spaced sections between diameters $D = 2 \cdot 10^{-4}$ μm and $D = 200$ μm.

[52] For Figure 1 we used two overlapping lognormal modes as the initial condition and the results show that we have excellent agreement for the number and mass distributions for this test case, which is representative of the simulation in section 5. The PartMC simulation exactly conserved total particle mass, and the particle number decreased by exactly the number of coagulation events that occurred. At the very largest sizes there was some noise in the particle-based mass distribution, as each individual particle had significant mass at these sizes. This noise could be reduced by averaging several simulations in a Monte Carlo fashion, or by using a variable number of physical particles per computational particle, as in the Mass Flow Algorithm [*Babovsky*, 1999; *Eibeck and Wagner*, 2001]. We do not consider this noise to be significant enough for the study in this paper to require amelioration.

[53] For the Brownian kernel in Figure 1 the use of the binned stochastic coagulation algorithm of section 4.3

improved the accept rate from 0.95% to 86%, requiring over 90 times fewer kernel evaluations. For a more non-uniform gravitational kernel, such as found in cloud-aerosol simulations, the binned algorithm increased the accept rate from 0.007% to 86%, a reduction of over 12,000 times in the number of kernel evaluations (not shown in a figure).

[54] To verify the stochastic treatment of emissions and dilution, we compared the PartMC algorithm against the analytical solution for constant mean emission and dilution rates. The PartMC simulation used a single run, 10^5 particles, and a $\Delta t = 1$ min time step (all identical to the simulation in section 5) and the results are shown in Figure 2. This test also shows excellent agreement. We thus see that PartMC-MOSAIC is performing emissions, dilution, and coagulation with accurate numerics, and it has been shown that the MOSAIC chemistry model is of similar or higher accuracy than other similar trace-gas and aerosol chemistry modules used in current state-of-the-art sectional and modal aerosol models [*Zaveri and Peters*, 1999; *Zaveri et al.*, 2005b, 2005a, 2008].

5. Application of PartMC-MOSAIC to an Idealized Urban Plume Scenario

5.1. Setup of Case Study

[55] For this study we considered an idealized urban plume scenario, which is not supposed to represent a particular location or episode. The purpose of choosing idealized conditions is to demonstrate the capabilities of the model described in section 3 while remaining simple enough so that the dominant effects can be understood.

[56] We tracked the evolution of gas phase species and aerosol particles in a Lagrangian air parcel that initially contained background air and was advected over and beyond a large urban area. The simulation started at 0600 local standard time (LST), and during the advection process, primary trace gases and aerosol particles from different sources were emitted into the air parcel for 12 h. After 1800 LST, the emissions were switched off, and the evolution of the air parcel was tracked for another 12 h.
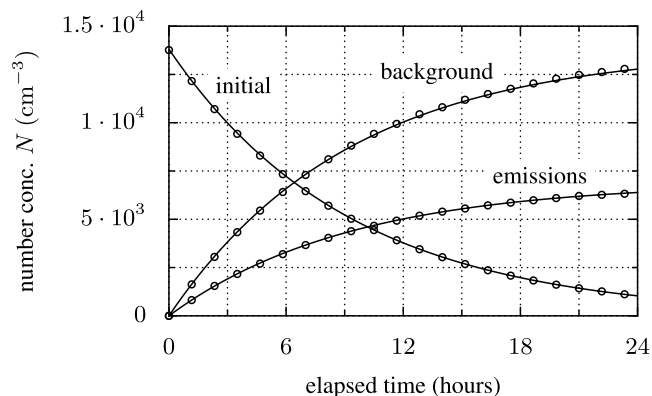

Figure 2. Comparison of the stochastic particle-resolved method using 10^5 particles (circles) against the analytical solution (lines) for a simulation with only initial particles and constant mean rate emissions and dilution with a background population.

Table 1. Gas Phase Emissions and Initial Conditions[a]

MOSAIC Species	Symbol	Initial Mole Fraction (ppb)	Emissions (nmol m^{-2} s^{-1})
Nitric oxide	NO	0.1	31.8
Nitrogen dioxide	NO$_2$	1.0	1.67
Nitric acid	HNO$_3$	1.0	
Ozone	O$_3$	50.0	
Hydrogen peroxide	H$_2$O$_2$	1.1	
Carbon monoxide	CO	21	291.3
Sulfur dioxide	SO$_2$	0.8	2.51
Ammonia	NH$_3$	0.5	6.11
Hydrogen chloride	HCl	0.7	
Methane	CH$_4$	2200	
Ethane	C$_2$H$_6$	1.0	
Formaldehyde	HCHO	1.2	1.68
Methanol	CH$_3$OH	0.12	0.28
Methyl hydrogen peroxide	CH$_3$OOH	0.5	
Acetaldehyde	ALD2	1.0	0.68
Paraffin carbon	PAR	2.0	96
Acetone	AONE	1.0	1.23
Ethene	ETH	0.2	7.2
Terminal olefin carbons	OLET	$2.3 \cdot 10^{-2}$	2.42
Internal olefin carbons	OLEI	$3.1 \cdot 10^{-4}$	2.42
Toluene	TOL	0.1	4.04
Xylene	XYL	0.1	2.41
Lumped organic nitrate	ONIT	0.1	
Peroxyacetyl nitrate	PAN	0.8	
Higher organic acid	RCOOH	0.2	
Higher organic peroxide	ROOH	$2.5 \cdot 10^{-2}$	
Isoprene	ISOP	0.5	0.23
Alcohols	ANOL		3.45

[a]The emissions represent area emissions and are averaged over the 12-h emission period. We obtain the volume emission rate $\vec{g}_{emit}(t)$ in equation (5) by dividing by the mixing height $H(t)$. Only those species are listed here that are initially present or emitted. Refer to *Zaveri and Peters* [1999] for more a detailed description of the species and reactions in the CBM-Z mechanism. Missing values indicate zero.

[57] Initial gas phase concentrations and emissions were adapted from the Southern California Air Quality Study (SCAQS) simulation (26–29 August 1988 period) of *Zaveri et al.* [2008], and are listed in Table 1. Note that while gas phase emissions in the simulation varied with time, Table 1 gives only the average over the emission period. The initial particle distribution, which was identical to the background aerosol distribution, was bimodal with Aitken and accumulation modes [*Jaenicke*, 1993]. We assumed that it consisted of (NH$_4$)$_2$SO$_4$ and primary organic aerosol (see Table 2). We considered three different types of carbonaceous aerosol emissions: (1) meat cooking aerosol, (2) diesel vehicle soot, and (3) gasoline vehicle soot. The parameters for the distributions of these three emission categories were based on work by *Eldering and Cass* [1996], *Kittelson et al.* [2006a], and *Kittelson et al.* [2006b], respectively. The emission rates

were adapted from the California Air Resources Board database (Emissions database: 2006 estimated annual average emissions, http://www.arb.ca.gov/ei/emissiondata.htm, accessed October 2007).

[58] For simplicity in this idealized study, the particle emissions strength and their size distribution and composition were kept constant with time during the time period of emission. This is certainly a substantial simplification as all these quantities in reality are expected to vary with time. However, for the purpose of this initial study it simplifies the interpretation of the results, while the capabilities of the model can still be demonstrated.

[59] Furthermore, we assumed that every particle from a given source had the same composition, with the species listed in Table 2, since to date the mixing state of particle emissions is still not well quantified. In particular, we assume that the diesel and gasoline exhaust particles consist exclusively of POA and BC, which is very nearly the case [*Andreae and Gelencsér*, 2006; *Medalia and Rivin*, 1982; *Kleeman et al.*, 2000]. At this point we do not have quantitative information on a single-particle basis of how the mean of this ratio depends on size or what the variance around this mean is, so we assigned all diesel particles a fixed BC/POA ratio and all gasoline particles a different fixed ratio. We also neglected any trace amounts of ionic species and metals, any variations with respect to vehicle operation, and any other particle types that may be present in the exhaust. For gasoline engines we took a BC dry-mass fraction of $w_{BC,dry} = 20\%$ based on page 5 of *Somers* [2004] (about 20% overall) and section 8.4, page 54, of *Nam et al.* [2008] (a composite figure of 17.3%). For diesel engines we used a BC dry mass fraction of $w_{BC,dry} = 70\%$, consistent with *Robert et al.* [2007] (73% for ultrafine particles and 61% for fine) and page 5 of *Somers* [2004] (about 50–80%).

[60] However, once quantitative particle composition data for emissions is available, it will be straightforward to use the information in our model. It would be valuable to have quantitative guidance on the particle-resolved composition of the main particle types that are identified in vehicle exhaust. Recent results [*Toner et al.*, 2006; *Shields et al.*, 2007] give very interesting particle-resolved composition data, but to date are qualitative only. Ideally, we would need for each type the mean size-resolved composition (mass fractions of BC, POA, ionic species, and metals) and an estimate of the variance around this mean due to vehicle-to-vehicle variations and variations in vehicle operation. Even without this level of detail, for our immediate interest in optical and CCN properties, valuable information would

Table 2. Aerosol Emissions and Initial Conditions[a]

Initial/Background	N (m^{-3})	D_{gn} (μm)	σ_g (1)	Composition by Mass
Aitken Mode	$3.2 \cdot 10^9$	0.02	1.45	50% (NH$_4$)$_2$SO$_4$, 50% POA
Accumulation Mode	$2.9 \cdot 10^9$	0.116	1.65	50% (NH$_4$)$_2$SO$_4$, 50% POA
Emissions	E (m^{-2} s^{-1})	D_{gn} (μm)	σ_g (1)	Composition by Mass
Meat cooking	$9 \cdot 10^6$	0.086	1.9	100% POA
Diesel vehicles	$1.6 \cdot 10^8$	0.05	1.7	30% POA, 70% BC
Gasoline vehicles	$5 \cdot 10^7$	0.05	1.7	80% POA, 20% BC

[a]Parameters are as defined in equation (23). The initial aerosol distribution is also used as the background aerosol distribution. The percentages for the composition are by mass. E is the area source strength of particle emissions. Dividing E by the mixing height $H(t)$ and multiplying by a normalized composition distribution gives the number distribution emission rate $\dot{n}_{emit}(\vec{\mu}, t)$ in equation (4).
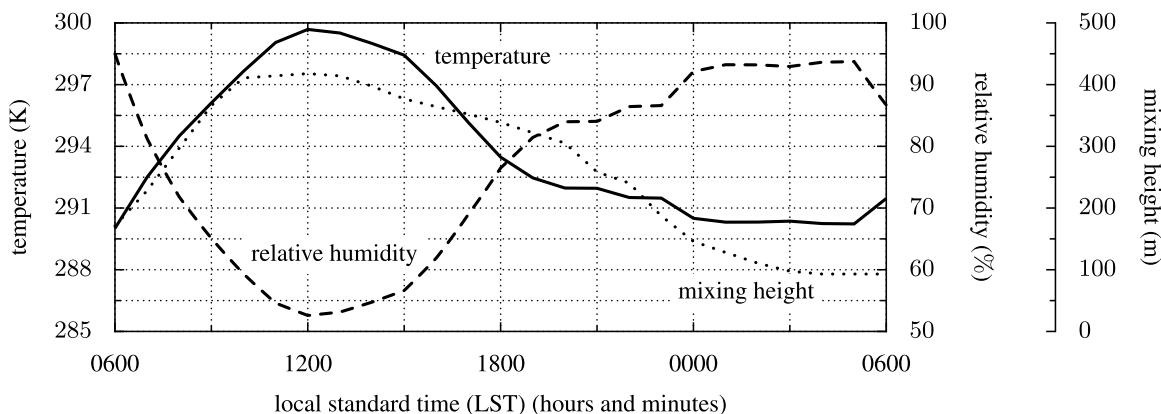
Figure 3. Time series of temperature, relative humidity, and mixing height over the course of the 24-h simulation. The pressure and water mixing ratio were kept constant.

consist of the particle-resolved absorbing to nonabsorbing fraction, and the soluble to insoluble fraction.

[61] Sea salt, biomass burning and mineral dust particles as well as particles from biological sources (e.g., pollen) were not treated in this test case.

[62] Before we discuss the results on aerosol mixing state in detail we provide the context for the conditions in our case study with Figures 3, 4, 5, and 6. The temperature, relative humidity, and mixing height along the trajectory were adapted from spatially averaged values from the Los Angeles Air Basin simulation of *Zaveri et al.* [2008] and references therein. It should be emphasized again that we did not attempt to simulate a specific episode or trajectory for the Los Angeles basin (as was done by *Kleeman et al.* [1997]), but rather an idealized urban plume scenario, with conditions that were consistent with a polluted environment. The temperature and mixing height were prescribed as functions of time, while the pressure and water mixing ratio were kept constant and the relative humidity and dry air density were updated accordingly. The variation of these parameters is shown in Figure 3. The relative humidity started at 95%, then decreased to 53% during the day and increased again to 94% during the following night. As we show below, the diurnal cycle of the ambient conditions impacted the thermodynamic equilibria and the phase states of the particles.

[63] An increase of the mixing height during the morning caused dilution of the gas and aerosol concentrations within the air parcel and was accompanied by entrainment of background air, as discussed in section 3.3. We also considered dilution due to horizontal turbulent diffusion, using a first-order dilution rate of $1.5 \cdot 10^{-5}$ s^{-1}, which corresponds to 5.4% per hour. Similar dilution rates have been observed in urban plumes [e.g., *Zaveri et al.*, 2003].

[64] We resolved the total aerosol distribution with 10^5 particles initially. The corresponding initial total number concentration was $N = 6100$ cm^{-3} and so the computational volume was initially $V = N_p/N = 16$ cm^3. It remained between $V = 8$ cm^3 and $V = 17$ cm^3 for the duration of the run as the number of particles N_p and number concentration N changed owing to emissions, dilution, and coagulation. The number of particles remained between $N_p = 60,481$ and $N_p = 199,949$. The time step used for this

simulation was $\Delta t = 1$ min (the same as for the verification studies in section 4.4). While better estimates of the system statistics could be obtained with multiple runs, we found a single run to give reasonable results in this case, as demonstrated in Figures 1 and 2 and discussed in section 4.4. Although not shown here, runs with different random initialization gave essentially the same results.

[65] To quantify the impact of coagulation we performed two runs, one base case including coagulation as described above, and one case without coagulation. Otherwise, the conditions for the two runs were identical.
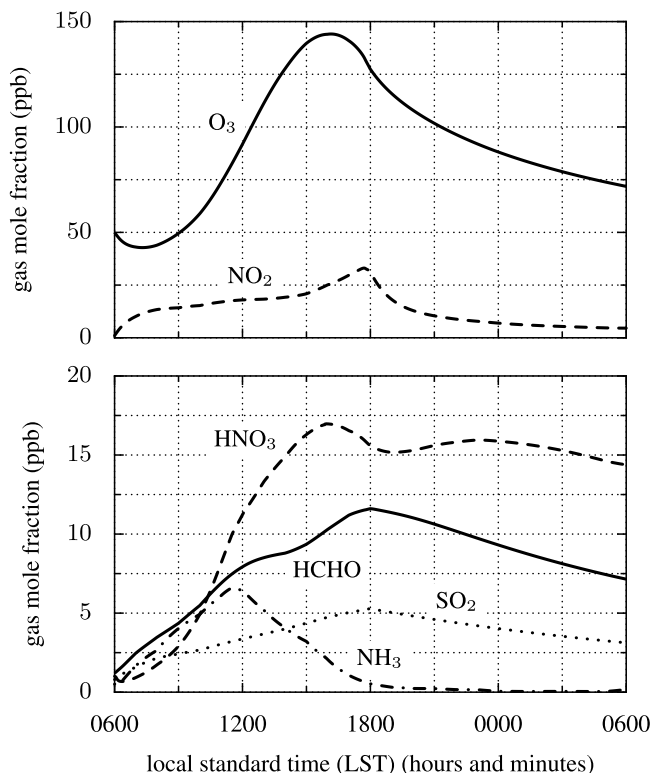

Figure 4. Time series of selected gas phase species. Gas phase emissions were present from 0600 to 1800 LST.
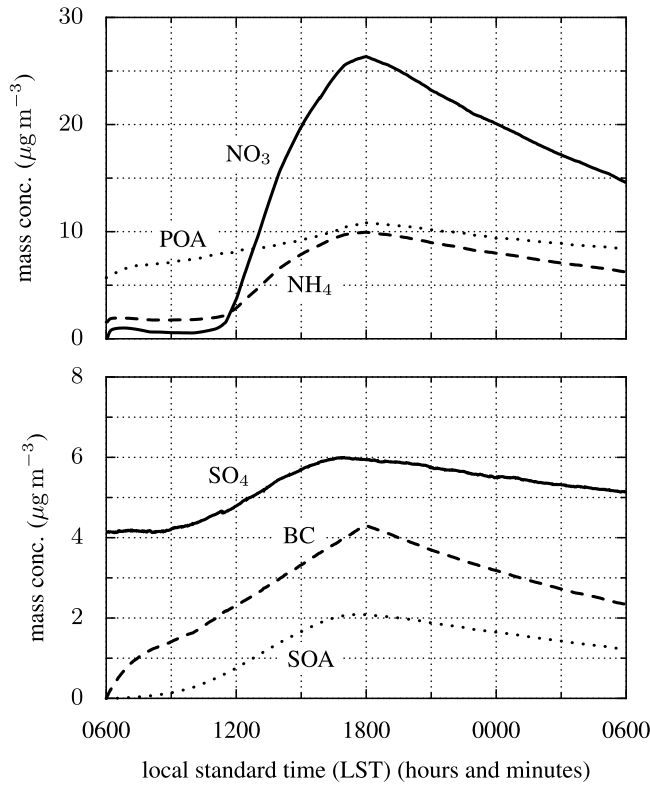
Figure 5. Time series of mass concentrations of selected aerosol species: M_{NO_3}, M_{NH_4}, M_{POA}, M_{SO_4}, M_{BC}, and M_{SOA}. Particle emissions were present from 0600 to 1800 LST.

5.2. Gas Species Evolution

[66] Figure 4 shows the evolution of selected gas phase species undergoing a diurnal cycle typical for a photochemistry episode under polluted conditions, measured as mole fractions in ppb (parts per billion, or number of trace gas molecules per 10^9 air molecules). During the daytime we observed a considerable production of O_3, reaching a maximum value of 144 ppb at 1609 LST. The NO_2 mole fraction increased up to 33 ppb during the time that NO_x was emitted, and decreased after 1800 LST owing to dilution and chemical reactions after the emissions had stopped. HNO_3 reached 17 ppb and contributed to the formation of ammonium nitrate in the particle phase. NH_3 levels reached 6.6 ppb during the daytime and later vanished owing to gas-to-particle conversion. HCHO was both emitted and chemically produced with a maximum value of 12 ppb at 1759 LST.

5.3. Bulk Aerosol Evolution

[67] Figure 5 shows time series of the bulk aerosol mass concentrations. We observed a pronounced production of ammonium nitrate, reaching nitrate mass concentration of up to 26 $\mu g\ m^{-3}$ and ammonium mass concentration of 10 $\mu g\ m^{-3}$ in the late afternoon. Sulfate mass concentrations increased from 4.1 $\mu g\ m^{-3}$ to 6.0 $\mu g\ m^{-3}$ owing to condensation of photochemically produced sulfuric acid. POA and BC were directly emitted (with a temporally constant rate) and accumulated to 11 $\mu g\ m^{-3}$ and 4.3 $\mu g\ m^{-3}$, respectively, until 1800 LST when the emissions

stopped. After 1800 LST the mass concentrations declined owing to dilution, especially nitrate and BC for which the background mass concentration was zero.

5.4. Aerosol Distribution Functions

[68] We take $N(D)$ (m^{-3}) to be the cumulative number distribution, giving the number of particles per volume that have diameter less than D. Similarly, the cumulative mass distribution $M(D)$ $(kg\ m^{-3})$ gives the mass per volume of particles with diameter less than D, while the per-species cumulative mass distribution $M_a(D)$ gives the mass per volume of species a in particles with diameter less than D. We write $N = N(\infty)$, $M = M(\infty)$, and $M_a = M_a(\infty)$ for the total number, mass, and per-species mass concentrations, respectively.

[69] Given the cumulative distributions, we define the number distribution $n(D)$ (m^{-3}), mass distribution $m(D)$ $(kg\ m^{-3})$ and per-species mass distribution $m_a(D)$ $(kg\ m^{-3})$ by

$$n(D) = \frac{dN(D)}{d\log_{10} D}, \tag{20}$$

$$m(D) = \frac{dM(D)}{d\log_{10} D}, \tag{21}$$

$$m_a(D) = \frac{dM_a(D)}{d\log_{10} D}. \tag{22}$$

The initial, background, and emitted number distributions used in this paper were all superpositions of lognormal distributions, each defined by

$$n(D) = \frac{N}{\sqrt{2\pi}\log_{10}\sigma_g} \exp\left(-\frac{\left(\log_{10} D - \log_{10} D_{gn}\right)^2}{2\left(\log_{10}\sigma_g\right)^2}\right), \tag{23}$$
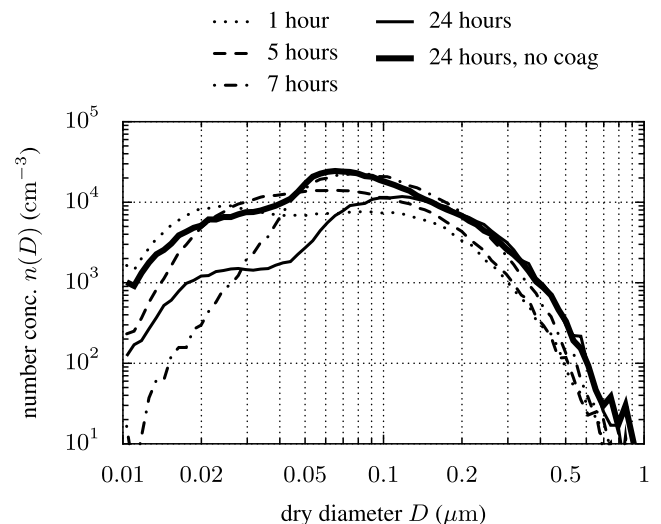

Figure 6. Number distributions $n(D)$ for the simulation with coagulation after 1, 5, 7, and 24 h, as defined in equation (20). For comparison the distribution without coagulation after 24 h is also shown.
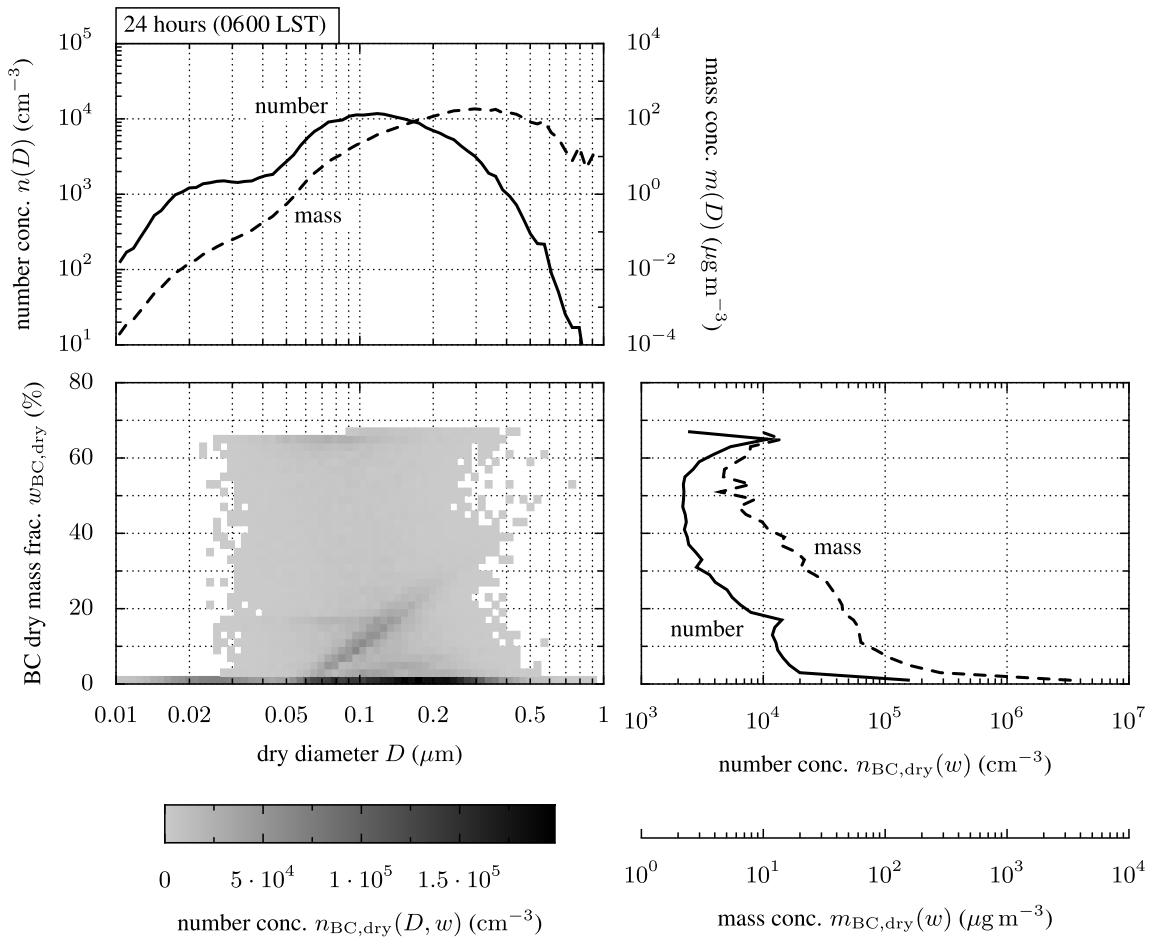
Figure 7. Number and mass distributions after 24 h of simulation (0600 LST the following day) with coagulation. (bottom left) Two-dimensional number distribution $n_{BC,dry}(D, w)$ defined in equation (28), and (top left and bottom right) corresponding one-dimensional distributions as functions of dry diameter D and BC dry mass fraction $w_{BC,dry}$, defined in equations (20) and (27), respectively.

where N (m^{-3}) is the number concentration, D_{gn} (m) is the geometric mean diameter, and σ_g (dimensionless) is the geometric standard deviation. To plot $n(D)$ and similar distributions from the particle-resolved output of PartMC-MOSAIC, we took a set of bins on the independent variable axis (D in this case) and counted the number or mass of particles that fall in each bin. In this paper we used 70 logarithmically spaced bins between $D = 0.01$ μm and $D = 1$ μm.

[70] To discuss the composition of a particle, we refer to certain mass fractions of species, as

$$w_{BC,POA} = \frac{\mu_{BC}}{\mu_{BC} + \mu_{POA}}, \qquad (24)$$

$$w_{BC,dry} = \frac{\mu_{BC}}{\mu_{dry}}, \qquad (25)$$

$$w_{H_2O,all} = \frac{\mu_{H_2O}}{\mu_{all}}, \qquad (26)$$

where we recall that μ_a (kg) is the mass of species a in a given particle, μ_{all} (kg) is the total wet mass of the particle, and $\mu_{dry} = \mu_{all} - \mu_{H_2O}$ (kg) is the total dry mass.

[71] We can define number and mass distributions as functions of mass fraction $w_{a,b}$ rather than of dry diameter D. That is, let $N_{a,b}(w)$ be the cumulative number distribution of particles with mass fraction of a to b less than w. The corresponding number distribution $n_{a,b}(w)$ is thus

$$n_{a,b}(w) = \frac{\partial N_{a,b}(w)}{\partial w}. \qquad (27)$$

The definition for mass distributions $M_{a,b}(w)$ (kg m^{-3}) and $m_{a,b}(w)$ (kg m^{-3}) are similar. The distributions as functions of w were plotted in the same way as $n(D)$ and $m(D)$. In this paper we used 40 bins between $w = 0\%$ and $w = 80\%$.

[72] The number and mass concentrations can be further extended to be functions of both particle composition and diameter. That is, the two-dimensional cumulative number distribution $N_{a,b}(w, D)$ (m^{-3}) is the number of particles per volume that have a diameter less than D and a mass ratio of species a to b less than w. The two-dimensional number distribution $n_{a,b}(D, w)$ (m^{-3}) is then defined by

$$n_{a,b}(D,w) = \frac{\partial^2 N_{a,b}(D,w)}{\partial \log_{10} D \, \partial w}. \qquad (28)$$

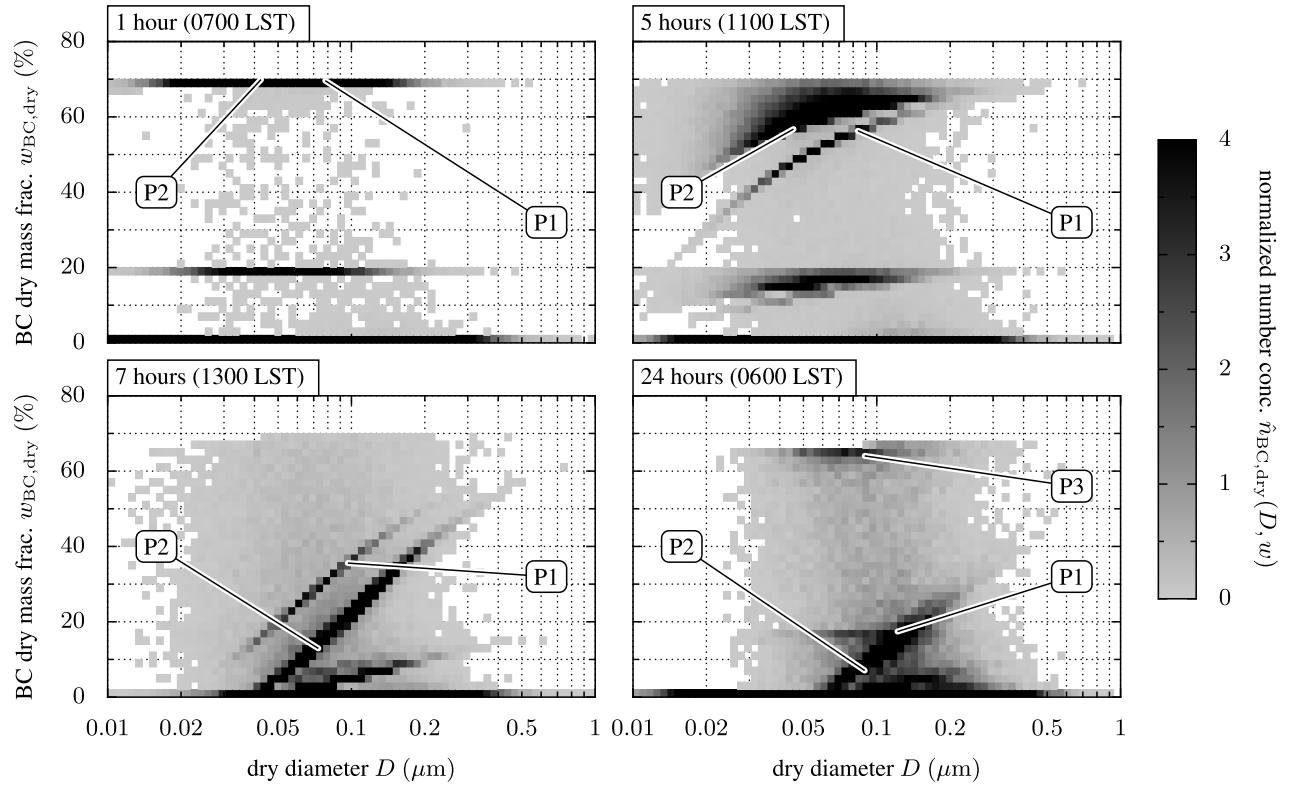**Figure 8.** Normalized two-dimensional number distribution $\hat{n}_{BC,dry}(D, w)$ (dimensionless) after 1, 5, 7, and 24 h of simulation with coagulation, as defined in equation (30). The labels P1, P2, and P3 track three individual diesel emission particles as they evolve over the course of the simulation, with compositions shown in Figure 10. The maximum plotted value for $\hat{n}_{BC,dry}(D, w)$ is capped at 4 to allow better resolution.

The two-dimensional cumulative mass distribution $M_{a,b}(D, w)$ (kg m^{-3}) and mass distribution $m_{a,b}(D, w)$ (kg m^{-3}) are defined similarly. To plot a two-dimensional distribution we formed a two-dimensional histogram by taking bins on both D and w axes and counting the number or mass of particles that fall within each bin pair. These quantities were then plotted as a color map, with no color if no particles were present in a given bin pair. We used the same sets of bins as for the one-dimensional distribution plots.

[73] We can also define two-dimensional distributions on the basis of other particle quantities. In particular, if we denote by k the number of coagulation events that a given particle has experienced during the simulation time then we can define the two-dimensional singly cumulative number distribution $N_{coag}(D, k)$ (m^{-3}) to be the number of particles per volume with diameter less than D and k coagulation events. Then $n_{coag}(D, k)$ (m^{-3}) is defined by

$$n_{coag}(D, k) = \frac{\partial N_{coag}(k, D)}{\partial \log_{10} D}. \qquad (29)$$

[74] For ease of comparison between different plots we frequently use normalized distributions denoted by a hat, so the normalized two-dimensional number distribution $\hat{n}_{a,b}(D, w)$ (dimensionless) is defined by

$$\hat{n}_{a,b}(D, w) = \frac{n_{a,b}(D, w)}{N}, \qquad (30)$$

and similarly for the mass distribution.

[75] We also find it convenient to plot one-dimensional mass distributions for certain composition ranges, as in Figure 14 in section 5.6. We write $m_{BC,dry}(D, [w_1, w_2])$ (kg m^{-3}) to refer to the mass distribution (including water) of particles for which $w_{BC,dry}$ is between w_1 and w_2, so that

$$m_{BC,dry}(D, [w_1, w_2]) = \int_{w_1}^{w_2} m_{BC,dry}(D, w)\, dw. \qquad (31)$$

5.5. Aerosol Size Distribution Evolution

[76] Figure 6 shows the number distribution $n(D)$ after 1, 5, 7, and 24 h of simulation including coagulation. For comparison, the result after 24 h of simulation without coagulation is also shown. The distribution after 1 h still resembled the bimodal initial distribution (compare Table 2), which was identical to the background distribution. After 5 h the distribution was primarily determined by the emissions. After 7 h condensation of secondary species (especially ammonium nitrate) caused substantial aerosol growth. In addition particles at small sizes were depleted owing to coagulation. After 24 h the Aitken mode of the background (as defined in Table 2) appeared again as a result of dilution.

[77] Compared to the distribution without coagulation, the distribution with coagulation showed a substantial decrease in number concentration for particles smaller than 0.1 μm. With coagulation the number concentration N started at $N = 6100$ cm^{-3}, then peaked at the end of
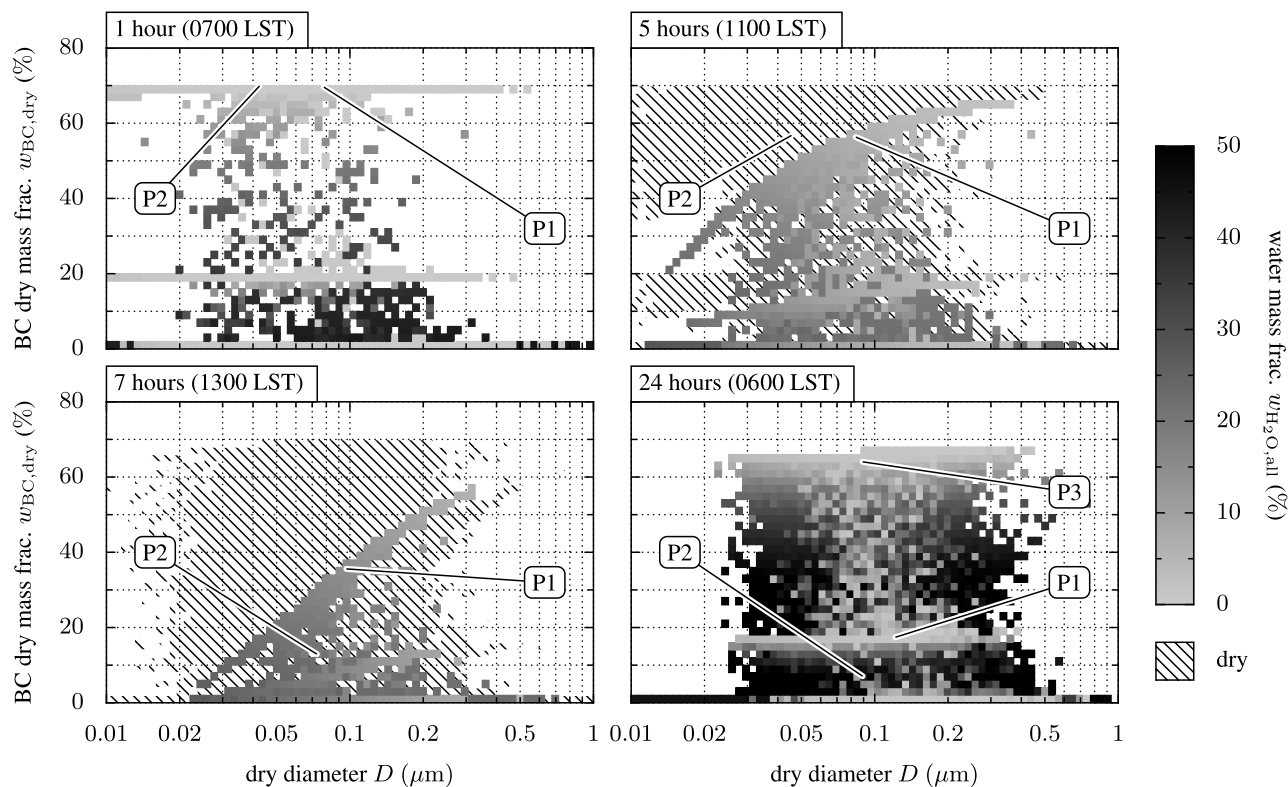
Figure 9. Water mass fraction $w_{H_2O,all}$ as a function of BC dry mass fraction $w_{BC,dry}$ and dry diameter D after 1, 5, 7, and 24 h of simulation with coagulation. The labels P1, P2, and P3 track three individual diesel emission particles as they evolve over the course of the simulation, with compositions shown in Figure 10. Note that the water fraction of wet particles is plotted over the hashing for dry particles and sometimes obscures it. In particular, after 1 h (0700 LST) there are dry diesel and gasoline particles present but they are not visible. The water fraction plotted for a given two-dimensional bin is the minimum of the water fraction for all wet particles in that bin. For example, after 24 h the particle P1 is very wet (see Figure 10) but there are much drier particles present with similar composition, giving a low $w_{H_2O,all}$ value on the plot at P1. The maximum plotted value for $w_{H_2O,all}$ is capped at 50% to allow better resolution.

the emission period after 12 h with a maximal value of 16,700 cm^{-3}. After this, N declined owing to coagulation and dilution to 7340 cm^{-3}. The simulation without coagulation started with the same initial number concentration, but the lack of coagulation lead to a maximum number concentration of 23,800 cm^{-3}, and a final value of 15,400 cm^{-3}. This means that coagulation decreased the peak and final number concentrations by 30% and 52%, respectively. Comparing the number distributions for the specific diameters $D = 0.03$, 0.05, 0.07, and 0.1 μm with and without coagulation, we find that coagulation decreased the number distribution $n(D)$ by 81%, 84%, 68%, and 36% respectively.

[78] We notice that for all number distributions shown in Figure 6 the results are somewhat noisy at small and large diameters. This noise is inherent to the stochastic model that is used for coagulation, dilution and emissions. Toward the edges of the size spectrum only a few particles are being used to represent the distribution owing to the low number concentration. Single particle variations arising from the stochastic model thus appear as a noisy curve. This could be rectified by averaging repeated Monte Carlo simulations or by using a variable number of physical particles per

computational particle, as in the Mass Flow Algorithm [*Babovsky*, 1999; *Eibeck and Wagner*, 2001].

5.6. Aerosol Mixing State Evolution

[79] While Figures 5 and 6 give an overview of aerosol size distribution and composition just like we obtain from traditional size-distribution-based models, they do not address the issue of mixing state. To elucidate how the mixing state evolved over the course of the simulation we display the data as shown in Figure 7, where the two-dimensional number distribution is plotted as a function of dry diameter and dry mass fraction of BC, $w_{BC,dry}$, in this case after 24 h of simulation (0600 LST the following day). Our definition of the two-dimensional number distribution is given in section 5.4. If we project the two-dimensional distribution onto the diameter axis, as shown in Figure 7 (top), then we obtain the regular size-resolved number distribution, as plotted in Figure 6. We can alternatively project onto the axis for BC dry mass fraction, giving the number distribution as a function of the mixing state $w_{BC,dry}$ as shown in Figure 7 (bottom right). We will discuss this representation in more detail for Figure 11 later in this section.
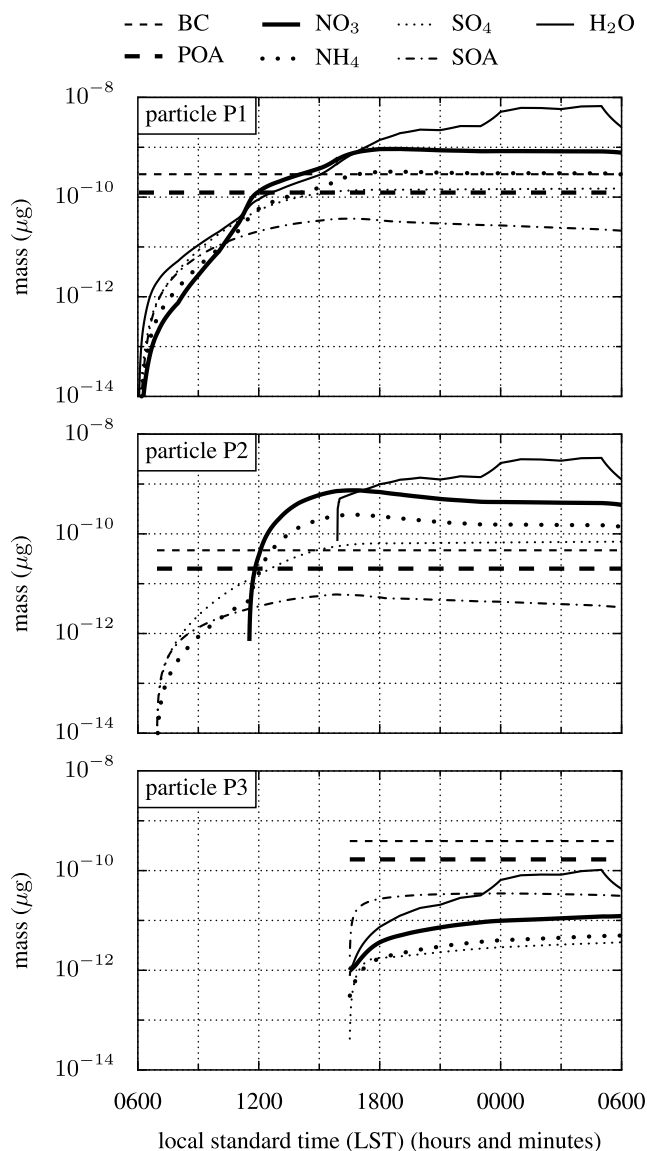
Figure 10. Time history of the composition of three individual diesel particles, P1, P2, and P3, from the simulation with coagulation. See Figures 8 and 9 for particle locations in size-composition space. P1 is emitted at 0603 LST and always contains water. P2 is emitted at 0657 LST and is initially dry but becomes wet in the afternoon. P3 is emitted at 1631 LST later in the day when little condensation occurs.

[80] Figure 8 shows the two-dimensional number distributions as a function of dry diameter and mass fraction of BC, $w_{BC,dry}$, after 1, 5, 7, and 24 h of simulation. This corresponds to local standard times 0700, 1100, 1300, and 0600 on the next morning.

[81] We will discuss the evolution of the two-dimensional number distribution in conjunction with Figure 9. The gray scale in Figure 9 shows the water mass fraction of the particles, $w_{H_2O,all}$, as a function of BC dry mass fraction, $w_{BC,dry}$, and particle size. We also include in Figure 10 the temporal evolution of the composition of three represen-

tative particles to aid the interpretation. These particles are labeled with P1, P2 and P3 in Figure 8. Their times of emission are 0603 LST, 0657 LST, and 1631 LST, respectively.

[82] Figure 8 shows the BC dry mass fraction, $w_{BC,dry}$, relative to all other dry constituents. Since even at the time of emission no particles were pure BC, particles were not present at $w_{BC,dry} = 100\%$. Fresh emissions from diesel vehicles ($w_{BC,dry} = 70\%$) and gasoline vehicles ($w_{BC,dry} = 20\%$) appear as horizontal lines since particles in one emission category were all emitted with the same composition. At $w_{BC,dry} = 0\%$ all the particles appear that do not contain any BC (i.e., background particles and particles from meat cooking emissions that have not undergone coagulation with particles containing BC). After 1 h (0700 LST) a small number of particles in between these three classes indicate the occurrence of coagulation.

[83] Under the initial ambient conditions the emitted diesel and gasoline particles accumulated small amounts of ammonium sulfate, ammonium nitrate and water. After 0642 LST the relative humidity fell below 85%, which is the deliquescence point of the inorganic mixture of ammonium, sulfate and nitrate. As a result of the hysteresis of particle deliquescence and crystallization, the particles that had been emitted up to this point stayed wet throughout the whole day (since the relative humidity never fell below the crystallization point), but freshly emitted particles were dry from this point in time onward until the relative humidity reached 61% in the afternoon at 1554 LST. Hence, between 0649 and 1554 LST, wet and dry particles coexisted in the air parcel. Particle P1 in Figures 8 and 9 is one of the particles that was emitted early and stayed wet throughout the simulation, whereas particle P2 started out dry and became wet only in the afternoon. For the wet and dry particles different thermodynamic equilibria applied which was reflected in the different development of their $w_{BC,dry}$ values.

[84] As the single-particle plot Figure 10 shows, the wet particles contained nitrate from the beginning and kept taking up nitrate, while during the first few hours vapor pressures of HNO_3 and NH_3 were too low to allow nitrate formation on dry particles. Owing to this difference in nitrate formation, after 5 h (1100 LST) the wet particles appear distinct from the dry particles in Figure 8 and reached lower $w_{BC,dry}$ values, reflecting their larger ammonium nitrate content.

[85] This changed after 1130 LST. At this time HNO_3 and NH_3 mole fractions were high enough that ammonium nitrate formed on the dry particles. They accumulated ammonium nitrate quickly, and $w_{BC,dry}$ decreased rapidly for the dry particles. As a result, $w_{BC,dry}$ of the dry particles fell below $w_{BC,dry}$ of the wet particles, as is evident in the plot for 7 h (1300 LST) in Figures 8 and 9.

[86] After 1800 LST the ammonium nitrate formation stopped, as the NH_3 mole fraction dropped to near zero (compare Figure 4). Therefore the fresh particle emissions after this time did not accumulate much condensable material and stayed at high $w_{BC,dry}$ values. This is reflected in the single-particle plot Figure 10, which shows the diesel particle P3 that was emitted in the afternoon. The mass of secondary species for this particle was much lower than its
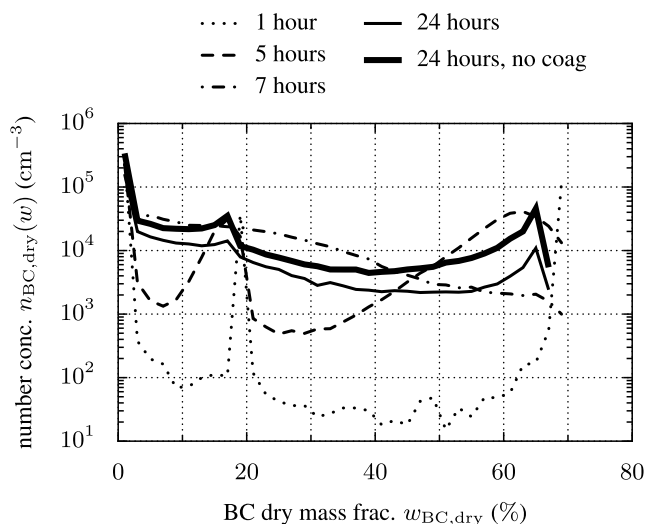
Figure 11. Number distributions $n_{BC,dry}(w)$ for the simulation with coagulation after 1, 5, 7, and 24 h, as defined in equation (27). For comparison the distribution without coagulation after 24 h is also shown.

BC content. After 12 h (1800 LST) both particle and gas emissions stopped, and the particle distribution changed mainly owing to coagulation and dilution. The particle number concentration decreased as a result of coagulation and continued dilution with the background, but this effect

is not visible in the normalized number distributions. During the evening hours the relative humidity increased again and particles took up a substantial amount of water. As the 24-h plot in Figure 9 shows, the water content depended on the mixing state, which in turn was determined by the history of the individual particles. For a given size we found particles with water mass fractions between near 0% and 66%.

[87] Comparing the result for the end of the simulation to the results at previous times, we note that at the end of the simulation particles below $D = 0.03$ μm were heavily depleted owing to coagulation. A continuum of mixing states formed in between the extreme mixing states of $w_{BC,dry} = 0\%$ and $w_{BC,dry} = 70\%$. It is also worth noting that the one-dimensional number distributions in Figure 6 appear quite similar above 0.1 μm at 7 and 24 h, but very different in the composition-resolved Figure 8.

[88] Figure 11 shows the projection of Figure 8 onto the axis for BC dry mass fraction, giving the number distribution as a function of the mixing state $w_{BC,dry}$. We see that after 1 h of simulation the emissions were concentrated at mixing ratios of $w_{BC,dry} = 0\%$, 20%, and 70%. As time progressed the intermediate mixing ratios filled in to within 1 order of magnitude at the end of the simulation.

[89] The comparison to the case without coagulation gives results as displayed in Figure 12. Figure 12 is analogous to Figure 8 and shows the mixing state $w_{BC,dry}$ of BC with respect to the sum of all other substances. Without coagulation, similar frontal features appeared, but

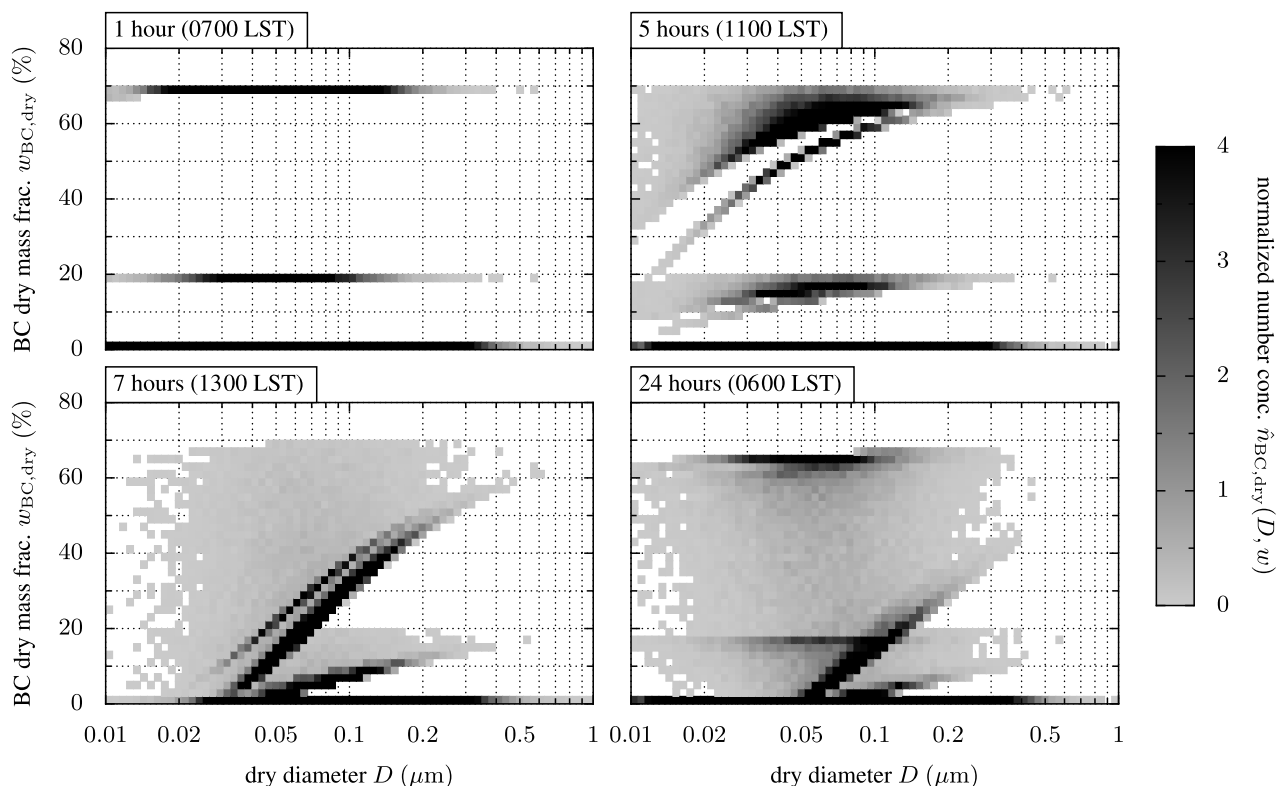**Figure 12.** Normalized two-dimensional number distribution $\hat{n}_{BC,dry}(D, w)$ (dimensionless) after 1, 5, 7, and 24 h of simulation, as in Figure 8, but for the simulation without coagulation. The maximum plotted value for $\hat{n}_{BC,dry}(D, w)$ is capped at 4 to allow better resolution.

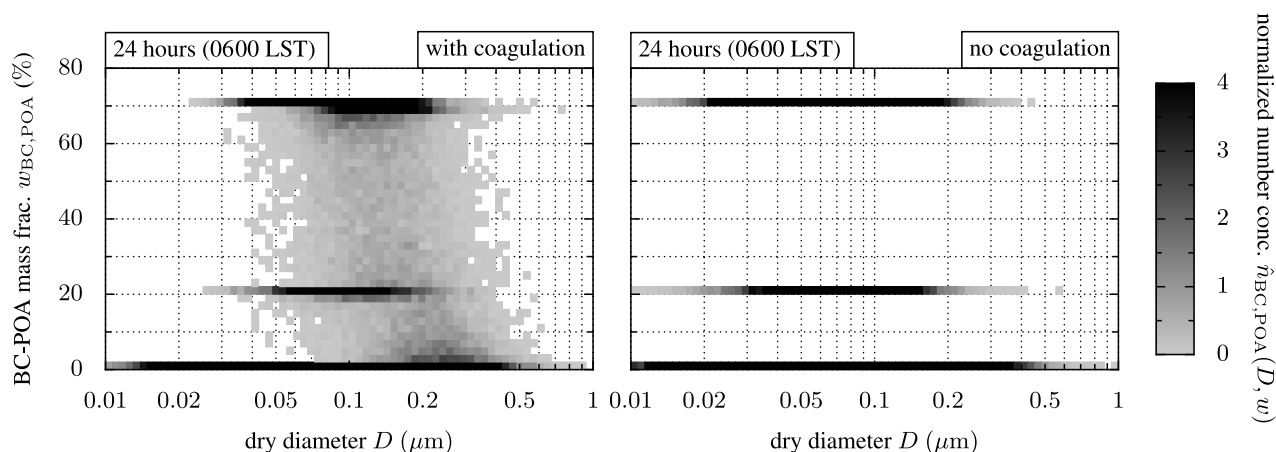**Figure 13.** Normalized two-dimensional number distribution $\hat{n}_{BC,POA}(D, w)$ (dimensionless) after 24 h of simulation (0600 LST the following day), with and without coagulation, as defined in equation (30). The maximum plotted value for $\hat{n}_{BC,POA}(D, w)$ is capped at 4 to allow better resolution.

diesel particles and gasoline particles remained more clearly distinct until 7 h of simulation (1300 LST) without the mixing effect of coagulation. Around 1300 LST the mixing state became continuous, because the most-aged diesel emissions started overlapping with the relatively fresh gasoline emission particles. However, since these mixing states were formed owing to condensation only, individual particles only contained both POA and BC if they were emitted as such. After 24 h of simulation without coagulation, mixed particles smaller than $D = 0.03$ μm were still present while they were depleted in Figure 8 with coagulation.

[90] The impact of coagulation on the mixing state with respect to the primary components BC and POA is shown in Figure 13. Figure 13 (left) displays the BC mixing state with respect to POA, $w_{BC,POA}$, after 24 h with coagulation. POA was emitted as a constituent of primary particles, which can be seen as horizontal lines with high number concentrations at $w_{BC,POA} = 70\%$ for diesel emissions, $w_{BC,POA} = 20\%$ for gasoline emissions and $w_{BC,POA} = 0\%$ for meat cooking emissions. The mixing states between these could only form as a result of coagulation. Since coagulation is most efficient between particles of different sizes, we observe that these mixed particles preferentially formed in a specific size range. For sizes larger than $D = 0.05$ μm, POA/BC mixtures of various degrees of mixing formed owing to coagulation. Below 0.05 μm coagulation produced very few particles so particles at these sizes were at their initial BC/POA mixing state. Nearly all BC-containing particles below 0.03 μm were removed by coagulation. For comparison, Figure 13 (right) shows the BC mixing state with respect to POA, $w_{BC,POA}$, at the end of the simulation without coagulation. For this case the intermediate mixing states did not occur, and BC-containing particles below $D = 0.03$ μm remained.

[91] Figure 14 shows the one-dimensional distributions of mass concentration (including water) for different ranges of mixing states at the end of the simulation, comparing the cases with and without coagulation. From this we see that coagulation did not simply reduce the number concentrations, but also shifted black carbon mass within the diameter-

$w_{BC,dry}$ space. The mass concentration of particles smaller than $D = 0.05$ μm with high BC content ($w_{BC,dry}$ between 60% and 70%) was reduced by 89% owing to coagulation. The mass concentration of particles smaller than $D = 0.05$ μm with very low BC content ($w_{BC,dry}$ between 0% and 2% BC) was reduced by 80% when coagulation was included. A very large difference between the cases with and without coagulation occurred for $w_{BC,dry}$ between 2% and 10% and for the size range above $D = 0.1$ μm. Mass in this range of parameters arose mainly from coagulation of large, BC-free particles with small BC-containing particles and this mass concentration increased by 426% when coagulation was included.

[92] With PartMC it is straightforward to track the number of coagulation events experienced by the individual
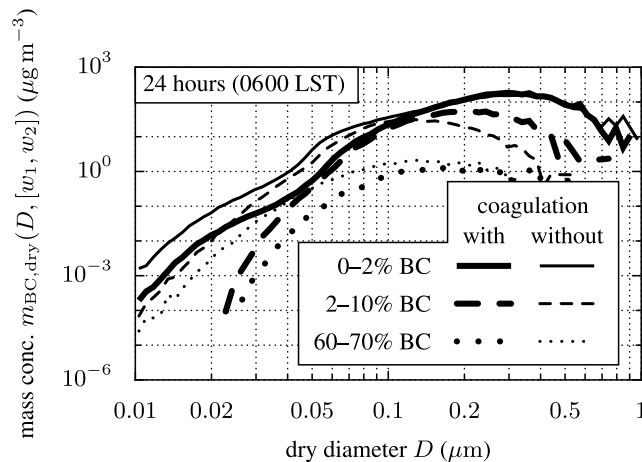

Figure 14. Mass distribution after 24 h (0600 LST the following day) for three different mixing state ranges: $m_{BC,dry}(D, [0\%, 2\%])$, $m_{BC,dry}(D, [2\%, 10\%])$, and $m_{BC,dry}(D, [60\%, 70\%])$, as defined in equation (31). The cases with and without coagulation are plotted for comparison.

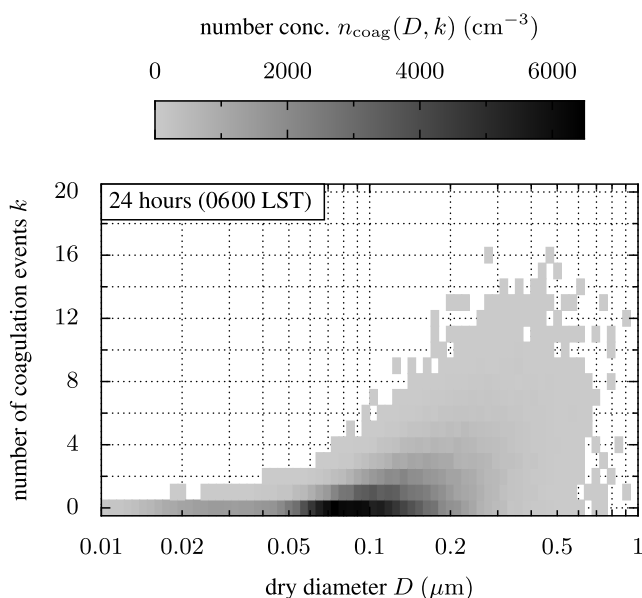number conc. $n_{\text{coag}}(D,k)$ (cm^{-3})

Figure 15. Two-dimensional number distribution $n_{\text{coag}}(D,k)$ showing the number of coagulation events experienced after 24 h (0600 LST the following day), as defined in equation (29).

particles. Figure 15 shows the two-dimensional number distribution $n(D, k)$, where k is the number of coagulation events. At the end of the simulation, 5% of particles had undergone at least five coagulation events. The trend was that particles that had experienced more coagulation events tended to be larger, with a maximum of 18 events for a single particle. Given a certain size, the number of coagulation events varied, which shows the stochastic nature of the coagulation process. The range of variation was greater for larger particles. For example, while the number of coagulation events varied between 0 and 7 for particles with $D = 0.1$ μm, it ranged between 0 and 13 for particles with $D = 0.3$ μm.

6. Summary

[93] In this paper we presented the development and application of a stochastic particle-resolved aerosol model, PartMC-MOSAIC. It explicitly resolves the composition of individual aerosol particles as the population evolves in time as a result of emission, dilution, condensation and coagulation. To make this computationally feasible we developed a new constant-time-step binned-sampling approach for stochastic coagulation with highly nonuniform coagulation kernels, such as the Brownian kernel over the atmospherically relevant aerosol size ranges. Owing to the explicit representation of mixing state on a per-particle level, PartMC-MOSAIC is suitable for use as a numerical benchmark of mixing state for more approximate models. The code for PartMC is available under the GNU General Public License (GPL) at http://lagrange.mechse.illinois.edu/mwest/partmc/, and the MOSAIC code is available upon request from R. A. Zaveri.

[94] We applied PartMC-MOSAIC to an idealized example urban plume case to simulate the aging process of black carbon in an evolving aerosol population. For the first time,

results of the aerosol composition and size distribution were available as a fully multidimensional distribution without any a priori assumptions about the evolution of the mixing state. This detail of information was only achievable with a particle-resolved model.

[95] To display the results, we projected the multidimensional mass and number distributions to two-dimensional distributions depending on particle size and BC mass ratio. We specifically discussed the results for BC mass ratios defined with respect to all other dry constituents, $w_{\text{BC,dry}}$, and to POA, $w_{\text{BC,POA}}$. Owing to the diurnal variations in temperature, relative humidity, and gas phase concentrations, the thermodynamic equilibrium conditions for the ammonium-sulfate-nitrate system changed continuously. The aerosol hydration hysteresis effect led to the coexistence of metastable (wet) and stable (dry) particles in the air parcel during the daytime, depending on their time of emission. Since the formation of ammonium nitrate depends on the particle phase state, this in turn resulted in pronounced differences in how the aging proceeded. As a result of coagulation and condensation, after 24 h of simulation the aerosol population evolved into a state where a continuum of BC mixing states existed. Coagulation was effective in removing smaller particles and in altering the distribution of mass in the space of mixing states.

[96] We emphasize that the primary value of the study in section 5 was to demonstrate the new model capabilities. We designed the urban plume scenario as a compromise in terms of simplicity while still reflecting processes that are relevant in reality. For future application it be will important to strengthen the connection of model results to physical reality by connecting PartMC-MOSAIC simulation results to direct measurements. This includes a more detailed treatment of the properties of individual particle emissions. In this regard it would be helpful to obtain quantitative information on the composition of the main particle classes that are present in the emissions categories being treated.

References

Adams, P. J., J. H. Seinfeld, and D. M. Koch (1999), Global concentration of tropospheric sulphate, nitrate and ammonium simulated in a general circulation model, *J. Geophys. Res.*, *104*, 13,791–13,823.

Alfonso, L., G. Raga, and D. Baumgardner (2008), Monte Carlo dimulations of two-component drop growth by stochastic coalescence, *Atmos. Chem. Phys. Discuss.*, *8*, 7289–7313.

Anderson, D. (2007), A modified next reaction method for simulating chemical systems with time dependent propensities and delays, *J. Chem. Phys.*, *127*, 214107, doi:10.1063/1.2799998.

Anderson, D. (2008), Incorporating postleap checks in tau-leaping, *J. Chem. Phys.*, *128*, 054103, doi:10.1063/1.2819665.

Andreae, M., and A. Gelencsér (2006), Black carbon or brown carbon? The nature of light-absorbing carbonaceous aerosols, *Atmos. Chem. Phys.*, *6*, 3131–3148.

Andreae, M. O., R. J. Charlson, F. Bruynseels, H. Storms, and R. V. Grieken (1986), Internal mixture of sea salt, silicates, and excess sulfate in marine aerosols, *Science*, *232*, 1620–1623.

Babovsky, H. (1999), On a Monte Carlo scheme for Smoluchowski's coagulation equation, *Monte Carlo Methods Appl.*, *5*, 1–18.

Bhave, P. V., M. J. Kleeman, J. O. Allen, and L. S. Hughes (2002), Evaluation of an air quality model for the size and composition of source-oriented particle classes, *Environ. Sci. Technol.*, *36*, 2154–2163.

Binkowski, F. S., and U. Shankar (1995), The regional particulate matter model: 1. Model description and preliminary results, *J. Geophys. Res.*, *100*, 26,191–26,209.

Bond, T. C., G. Habib, and R. W. Bergstrom (2006), Limitations in the enhancement of visible light absorption due to mixing state, *J. Geophys. Res.*, *111*, D20211, doi:10.1029/2006JD007315.

Bott, A. (1998), A flux method for the numerical solution of the stochastic collection equation, *J. Atmos. Sci.*, *55*, 2284–2293.

Brock, J. R., P. J. Kuhn, and D. Zehavi (1988), Formation and growth of binary aerosol in a laminar coaxial jet, *J. Aerosol Sci.*, *19*, 413–424.

Burtscher, H., S. Künzel, and C. Hügling (1998), Characterization of particles in combustion engine exhaust, *J. Aerosol Sci.*, *29*, 389–396.

Cao, Y., D. T. Gillespie, and L. R. Petzold (2005), The slow-scale stochastic simulation algorithm, *J. Chem. Phys.*, *122*, 014116, doi:10.1016/j.jcp.2004.12.014.

Cao, Y., D. T. Gillespie, and L. R. Petzold (2006), Efficient stepsize selection for the tau-leaping simulation method, *J. Chem. Phys.*, *124*, 044109, doi:10.1063/1.2159468.

Chung, S. H., and J. H. Seinfeld (2002), Global distribution and climate forcing of carbonaceous aerosols, *J. Geophys. Res.*, *107*(D19), 4407, doi:10.1029/2001JD001397.

Chung, S. H., and J. H. Seinfeld (2005), Climate response of direct radiative forcing of anthropogenic black carbon, *J. Geophys. Res.*, *111*, D11102, doi:10.1029/2004JD005441.

Chýlek, P., G. Videen, D. Ngo, R. G. Pinnek, and J. D. Klett (1995), Effect of black carbon on the optical properties and climate forcing of sulfate aerosols, *J. Geophys. Res.*, *100*, 16,325–16,332.

Clarke, A. D., and K. J. Noone (1985), Soot in the Arctic snowpack: A cause for pertubations in radiative transfer, *Atmos. Environ.*, *19*, 2045–2053.

Cooke, W. F., C. Liousse, H. Cachier, and J. Feichter (1999), Construction of a 1° × 1° fossil fuel emission data set for carbonaceous aerosol and implementation and radiative impact in the ECHAM4 model, *J. Geophys. Res.*, *104*, 22,137–22,162.

Croft, B., U. Lohmann, and K. von Salzen (2005), Black carbon aging in the Canadian Centre for Climate modelling and analysis atmospheric general circulation model, *Atmos. Chem. Phys.*, *5*, 1931–1949.

Cubison, M. J., B. Ervens, G. Feingold, K. S. Docherty, I. M. Ulbrich, L. Shields, K. Prather, S. Hering, and J. L. Jimenez (2008), The influence of chemical composition and mixing state on Los Angeles urban aerosol on CCN number and cloud properties, *Atmos. Chem. Phys. Discuss.*, *8*, 5629–5681.

Debry, E., B. Sportisse, and B. Jourdain (2003), A stochastic approach for the numerical simulation of the general dynamics equations for aerosols, *J. Comput. Phys.*, *184*, 649–669, doi:10.1016/S0021-9991(02)00041-4.

Dhaniyala, S., and A. S. Wexler (1996), Numerical schemes to model condensation and evaporation of aerosols, *Atmos. Environ.*, *30*, 919–928.

Dreher, K., R. Jaskot, J. Lehmann, J. Richards, J. McGee, A. Ghio, and D. Costa (1997), Soluble transition metals mediate residual oil fly ash induced acute lung injury, *J. Toxicol. Environ. Health*, *50*, 285–305.

Ducret, J., and H. Cachier (1992), Particulate carbon in rain at various temperate and tropical locations, *J. Atmos. Chem.*, *15*, 55–67.

E, W., D. Liu, and E. Vanden-Eijnden (2007), Nested stochastic simulation algorithm for chemical kinetic systems with multiple time scales, *J. Comput. Phys.*, *221*, 158–180.

Efendiev, Y., and M. R. Zachariah (2002), Hybrid Monte Carlo method for simulation of two-component aerosol coagulation and phase segregation, *J. Colloid Interface Sci.*, *249*, 30–43, doi:10.1006/jcis.2001.8114.

Eibeck, A., and W. Wagner (2001), Stochastic particle approximation for Smoluchowski's coagulation equation, *Ann. Appl. Probab.*, *11*(4), 1137–1165, doi:10.1214/aoap/1015345398.

Eldering, A., and G. R. Cass (1996), Source-oriented model for air pollution effects on visibility, *J. Geophys. Res.*, *101*, 19,343–19,369.

El Samad, H., M. Khammash, L. Petzold, and D. Gillespie (2005), Stochastic modeling of gene regulatory networks, *Int. J. Robust Nonlinear Control*, *15*(15), 691–711.

Erel, Y., S. O. Pehkonen, and M. R. J. Hoffmann (1993), Redox chemistry of iron in fog and stratus clouds, *J. Geophys. Res.*, *98*, 18,423–18,434.

Fassi-Fihri, A., K. Suhre, and R. Rosset (1997), Internal and external mixing in atmospheric aerosols by coagulation: Impact on the optical and hygroscopic properties of the sulphate-soot system, *Atmos. Environ.*, *31*, 1393–1402.

Fichthorn, K. A., and W. H. Weinberg (1991), Theoretical foundations of dynamical Monte Carlo simulations, *J. Chem. Phys.*, *95*, 1090–1096.

Garcia, A. L., C. van den Broek, M. Aertsens, and R. Serneels (1987), A Monte Carlo method of coagulation, *Physica A*, *143*, 535–546.

Gibson, M., and J. Bruck (2000), Efficient exact stochastic simulation of chemical systems with many species and many channels, *J. Phys. Chem. A*, *104*, 1876–1889.

Gillespie, D. T. (1972), The stochastic coalescence model for cloud droplet growth, *J. Atmos. Sci.*, *29*, 1496–1510.

Gillespie, D. T. (1975), An exact method for numerically simulating the stochastic coalescence process in a cloud, *J. Atmos. Sci.*, *32*, 1977–1989.

Gillespie, D. T. (1976), A general method for numerically simulating the stochastic time evolution of coupled chemical reactions, *J. Comput. Phys.*, *22*, 403–434.

Gillespie, D. T. (1977), Exact stochastic simulation of coupled chemical reactions, *J. Phys. Chem.*, *81*, 2340–2361, doi:10.1021/j100540a008.

Gillespie, D. T. (1992), *Markov Processes: An Introduction for Physical Scientists*, Academic Press, San Diego, Calif.

Gillespie, D. T. (2001), Approximate accelerated stochastic simulation of chemically reacting systems, *J. Chem. Phys.*, *115*, 1716–1733.

Gillespie, D. T. (2007), Stochastic simulation of chemical kinetics, *Annu. Rev. Phys. Chem.*, *58*, 35–55, doi:10.1146/annurev.physchem.58.032806.104637.

Gillespie, D. T., and L. R. Petzold (2003), Improved leap-size selection for accelerated stochastic simulation, *J. Chem. Phys.*, *119*, 8229, doi:10.1063/1.1613254.

Guias, F. (1997), A Monte Carlo approach to the Smoluchowski equations, *Monte Carlo Methods Appl.*, *3*, 313–326.

Hansen, J., and L. Nazarenko (2004), Soot climate forcing via snow and ice albedos, *Proc. Natl. Acad. Sci. U. S. A.*, *101*, 423–428.

Horvath, H., and A. Trier (1993), A study of the aerosol of Santiago de Chile: I. Light extinction coefficient, *Atmos. Environ.*, *27*, 371–384.

Jacobson, M. Z. (1997), Development and application of a new air pollution modeling system: II. Aerosol module structure and design, *Atmos. Environ.*, *31*, 131–144.

Jacobson, M. Z. (1999), *Fundamentals of Atmospheric Modeling*, Cambridge Univ. Press, Cambridge, U. K.

Jacobson, M. Z. (2000), A physically based treatment of elemental carbon optics: Implications for global direct forcing of aerosols, *Geophys. Res. Lett.*, *27*, 217–220.

Jacobson, M. Z. (2001), Strong radiative heating due to the mixing state of black carbon in atmospheric aerosols, *Nature*, *409*, 695–697.

Jacobson, M. Z. (2002a), Analysis of aerosol interactions with numerical techniques for solving coagulation, nucleation, condensation, dissolution, and reversible chemistry among multiple size distributions, *J. Geophys. Res.*, *107*(D19), 4366, doi:10.1029/2001JD002044.

Jacobson, M. Z. (2002b), Control of fossil-fuel particulate black carbon and organic matter, possibly the most effective method of slowing global warming, *J. Geophys. Res.*, *107*(D19), 4410, doi:10.1029/2001JD001376.

Jaenicke, R. (1993), Tropospheric aerosols, in *Aerosol-Cloud-Climate Interaction*, pp. 1–31, Academic Press, San Diego, Calif.

Johnson, K. S., B. Zuberi, L. T. Molina, M. J. Molina, M. J. Iedema, J. P. Cowin, D. J. Gaspar, C. Wang, and A. Laskin (2005), Processing of soot in an urban environment: Case study from the Mexico City metropolitan area, *Atmos. Chem. Phys.*, *5*, 3033–3043.

Kittelson, D., W. Watts, and J. Johnson (2006a), On-road and laboratory evaluation of combustion aerosols—Part 1: Summary of diesel engine results, *J. Aerosol Sci.*, *37*, 913–930.

Kittelson, D., W. Watts, J. Johnson, J. Schauer, and D. Lawson (2006b), On-road and laboratory evaluation of combustion aerosols—Part 2: Summary of spark ignition engine results, *J. Aerosol Sci.*, *37*, 931–949.

Kleeman, M. J., and G. R. Cass (1998), Source contributions to the size and composition distribution of urban particulate air pollution, *Atmos. Environ.*, *32*, 2803–2816.

Kleeman, M. J., G. R. Cass, and A. Eldering (1997), Modeling the airborne particle complex as a source-oriented external mixture, *J. Geophys. Res.*, *102*, 21,355–21,372.

Kleeman, M. J., L. S. Hughes, J. Allen, and G. R. Cass (1999), Source contributions to the size and composition distribution of atmospheric particles: Southern California in September 1996, *Environ. Sci. Technol.*, *33*, 4331–4341.

Kleeman, M. J., J. Schauer, and G. Cass (2000), Size and composition distribution of fine particulate matter emitted from motor vehicles, *Environ. Sci. Technol.*, *34*, 1132–1142, doi:10.1021/es981276y.

Kleeman, M. J., A. Eldering, J. R. Hall, and G. R. Cass (2001), Effect of emissions control programs on visibility in Southern California, *Environ. Sci. Technol.*, *35*, 4668–4674.

Koch, D. (2001), Transport and direct radiative forcing of carbonaceous and sulfate aerosols in the GISS GCM, *J. Geophys. Res.*, *106*, 20,311–20,332.

Kolodko, A., and K. Sabelfeld (2003), Stochastic particle methods for Smoluchowski coagulation equation: Variance reduction and error estimations, *Monte Carlo Methods Appl.*, *9*, 315–339, doi:10.1163/156939603322601950.

Kruis, F. E., A. Maisels, and H. Fissan (2000), Direct simulation Monte Carlo method for particle coagulation and aggregation, *AIChE J.*, *46*, 1735–1742.

Laurenzi, I. J., J. D. Bartels, and S. L. Diamond (2002), A general algorithm for exact simulation of multicomponent aggregation processes, *J. Comput. Phys.*, *177*, 418–449, doi:10.1006/jcph.2002.7017.

Lesins, G., P. Chýlek, and U. Lohmann (2002), A study of internal and external mixing scenarios and its effect on aerosol optic properties and direct radiative forcing, *J. Geophys. Res.*, *107*(D10), 4094, doi:10.1029/2001JD000973.

Levin, Z. L., E. Ganor, and V. Gladstein (1996), The effects of desert particles coated with sulfate on rain formation in the eastern Mediterranean, *J. Appl. Meteorol.*, *35*, 1511–1523.

Lohmann, U., J. Feichter, C. C. Chuang, and J. E. Penner (1999), Prediction of the number of cloud droplets in the ECHAM GCM, *J. Geophys. Res.*, *104*, 9169–9198.

Maisels, A., F. E. Kruis, and H. Fissan (2004), Direct simulation Monte Carlo for simultaneous nucleation, coagulation, and surface growth in dispersed systems, *Chem. Eng. Sci.*, *59*, 2231–2239.

McGraw, R. (1997), Description of aerosol dynamics by the quadrature method of moments, *Aerosol Sci. Technol.*, *27*, 255–265.

McGraw, R., L. Leng, W. Zhu, N. Riemer, and M. West (2008), Aerosol dynamics using the quadrature method of moments: Comparing several quadrature schemes with particle-resolved simulation, *J. Phys. Conf. Ser.*, *125*, 012020, doi:10.1088/1742-6596.

Medalia, A., and D. Rivin (1982), Particulate carbon and other components of soot and carbon black, *Carbon*, *20*, 481–492.

Menon, S., J. Hansen, L. Nazarenko, and Y. F. Luo (2002), Climate effects of black carbon aerosols in China and India, *Science*, *297*, 2250–2253.

Nam, E., C. Fulper, J. Warila, J. Somers, H. Michaels, R. Baldauf, R. Rykowski, and C. Scarbro (2008), Analysis of particulate matter emissions from light-duty gasoline vehicles in Kansas City, *Tech. Rep. EPA420-R-08-010*, 85 pp., Environ. Prot. Agency, Washington, D. C.

Nenes, A., W. C. Conant, and J. H. Seinfeld (2002), Black carbon radiative heating effects on cloud microphysics and implications for the aerosol indirect effect: 2. Cloud microphysics, *J. Geophys. Res.*, *107*(D21), 4605, doi:10.1029/2002JD002101.

Okada, K., and R. M. Hitzenberger (2001), Mixing properties of individual submicrometer aerosol particles in Vienna, *Atmos. Environ.*, *35*, 5617–5628.

Penner, J. E. (1995), Carbonaceous aerosols influencing atmospheric radiation: Black and organic carbon, in *Aerosol Forcing and Climate*, pp. 91–108, John Wiley, Hoboken, N. J.

Pope, A., and D. Dockery (1996), Epidemiology of chronic health effects: Cross-sectional studies, in *Particles in Our Air: Concentrations and Health Effects*, edited by R. W. und J. Sprengler, pp. 149–168, Harvard Univ. Press, Cambridge, Mass.

Press, W. H., S. A. Teukolsky, W. T. Vetterling, and B. P. Flannery (2007), *Numerical Recipes: The Art of Scientific Computing*, third ed., Cambridge Univ. Press, New York.

Rathinam, M., L. R. Petzold, Y. Cao, and D. T. Gillespie (2003), Stiffness in stochastic chemically reacting systems: The implicit tau-leaping method, *J. Chem. Phys.*, *119*, 12,784–12,794, doi:10.1063/1.1627396.

Riemer, N., H. Vogel, B. Vogel, and F. Fiedler (2003), Modeling aerosols on the mesoscale γ: 1. Treatment of soot aerosol and its radiative effects, *J. Geophys. Res.*, *108*(D19), 4601, doi:10.1029/2003JD003448.

Robert, M. A., M. J. Kleeman, and C. A. Jakober (2007), Size and composition distributions of particulate matter emissions: Part 2—Heavy-duty diesel vehicles, *J. Air Waste Manage. Assoc.*, *57*, 1429–1438, doi:10.3155/1047-3289.57.12.1429.

Roeckner, E., P. Stier, J. Feichter, S. Kloster, M. Esch, and I. Fischer-Bruns (2006), Impact of carbonaceous aerosol emissions on regional climate change, *Clim. Dyn.*, *27*, 553–571.

Saathoff, H., K.-H. Naumann, N. Riemer, S. Kamm, O. Möhler, U. Schurath, H. Vogel, and B. Vogel (2001), The loss of NO_2, HNO_3, NO_3/N_2O_5, and $HO_2/HOONO_2$ on soot aerosol: A chamber and modeling study, *Geophys. Res. Lett.*, *28*, 1957–1960.

Schell, B., I. J. Ackermann, F. S. Binkowski, and A. Ebel (2001), Modeling the formation of secondary organic aerosol within a comprehensive air quality model system, *J. Geophys. Res.*, *106*, 28,275–28,293.

Schnaiter, M., C. Linke, O. Möhler, K.-H. Naumann, H. Saathoff, R. Wagner, and B. Wehner (2005), Absorption amplification of black carbon internally mixed with secondary organic aerosol, *J. Geophys. Res.*, *110*, D19204, doi:10.1029/2005JD006046.

Shields, L., D. Suess, and K. Prather (2007), Determination of single particle mass spectral signatures from heavy-duty diesel vehicle emissions for PM2.5 source apportionment, *Atmos. Environ.*, *41*, 3841–3852.

Somers, J. (2004), Mobile source black carbon emissions, paper presented at Black Carbon Emissions and Climate Change: A Technical Workshop, U. S. Environ. Prot. Agency, Washington, D. C.

Spencer, M., and K. Prather (2006), Using ATOFMS to determine OC/EC mass fractions in particles, *Aerosol Sci. Technol.*, *40*, 585–594.

Spouge, J. L. (1985), Monte Carlo results for random coagulation, *J. Colloid Interface Sci.*, *107*(1), 38–43.

Stier, P., et al. (2005), The aerosol-climate model ECHAM5-HAM, *Atmos. Chem. Phys.*, *5*, 1125–1156.

Toner, S., S. Sodeman, and K. Prather (2006), Single particle characterization of ultrafine and accumulation mode particles from heavy duty diesel vehicles using aerosol time-of-flight mass spectrometry, *Environ. Sci. Technol.*, *40*, 3912–3921, doi:10.1021/es051455x.

Tsigaridis, K., and M. Kanakidou (2003), Global modeling of secondary organic aerosol in the troposphere: A sensitivity analysis, *Atmos. Chem. Phys.*, *3*, 1849–1869.

von Smoluchowski, M. (1916a), Drei Vorträge über Diffusion, Brownsche Molekularbewegung und Koagulation von Kolloidteilchen, *Phys. Z.*, *17*, 557–571, 585–599.

von Smoluchowski, M. (1916b), Versuch einer mathematischen Theorie der Koagulationskinetik kolloider Lösungen, *Z. Phys. Chem.*, *92*, 129–168.

Weingartner, E., H. Burtscher, and H. Baltensperger (1997), Hygroscopic properties of carbon and diesel soot particles, *Atmos. Environ.*, *31*, 2311–2327.

Wells, C., N. Morgan, M. Kraft, and W. Wagner (2006), A new method for calculating the diameters of partially-sintered nanoparticles and its effect on simulated particle properties, *Chem. Eng. Sci.*, *61*, 158–166.

Wexler, A. S., F. W. Lurmann, and J. H. Seinfeld (1994), Modelling urban aerosols—I. Model development, *Atmos. Environ.*, *28*, 531–546.

Whitby, E. R., and P. H. McMurry (1997), Modal aerosol dynamics modeling, *Aerosol Sci. Technol.*, *27*, 673–688.

Whitby, E. R., P. H. McMurray, U. Shankar, and F. S. Binkowski (1991), Modal Aerosol dynamics modeling, *Tech. Rep. 600/3-91/020*, Atmos. Res. and Exposure Assess. Lab., U.S. Environ. Prot. Agency, Research Triangle Park, N. C.

Wilson, J., C. Cuvelier, and F. Raes (2001), A modeling study of global mixed aerosol fields, *J. Geophys. Res.*, *106*, 34,081–34,108.

Wu, C.-Y., and P. Biswas (1998), Study of numerical diffusion in a discrete-sectional model and its application to aerosol dynamics simulation, *Aerosol Sci. Technol.*, *29*, 359–378.

Ying, Q., and M. J. Kleeman (2006), Source contributions to the regional distribution of secondary particulate matter in California, *Atmos. Environ.*, *40*, 736–752.

Ying, Q., M. Mysliviec, and M. J. Kleeman (2004), Source apportionment of visibility impairment using a three-dimensional source-oriented air quality model, *Environ. Sci. Technol.*, *38*, 1089–1101.

Yoon, C., and R. McGraw (2004a), Representation of generally mixed multivariate aerosols by the quadrature method of moments: I. Statistical foundation, *J. Aerosol Sci.*, *35*, 561–576, doi:10.1016/j.jaerosci.2003.11.003.

Yoon, C., and R. McGraw (2004b), Representation of generally mixed multivariate aerosols by the quadrature method of moments: II. Aerosol dynamics, *J. Aerosol Sci.*, *35*, 577–598, doi:10.1016/j.jaerosci.2003.11.012.

Zaveri, R. A., and L. K. Peters (1999), A new lumped structure photochemical mechanism for large-scale applications, *J. Geophys. Res.*, *104*, 30,387–30,415.

Zaveri, R. A., C. M. Berkowitz, L. I. Kleinman, S. R. Springston, P. V. Doskey, W. A. Lonneman, and S. W. Spicer (2003), Ozone production efficiency and NO_x depletion in an urban plume: Interpretation of field observations and implications for evaluating O_3-NO_x-VOC sensitivity, *J. Geophys. Res.*, *108*(D14), 4436, doi:10.1029/2002JD003144.

Zaveri, R. A., R. C. Easter, and L. K. Peters (2005a), A computationally efficient Multicompoennt Equilibrium Solver for Aerosols (MESA), *J. Geophys. Res.*, *110*, D24203, doi:10.1029/2004JD005618.

Zaveri, R. A., R. C. Easter, and A. S. Wexler (2005b), A new method for multicomponent activity coefficients of electrolytes in aqueous atmospheric aerosols, *J. Geophys. Res.*, *110*, D02201, doi:10.1029/2004JD004681.

Zaveri, R. A., R. C. Easter, J. D. Fast, and L. K. Peters (2008), Model for Simulating Aerosol Interactions and Chemistry (MOSAIC), *J. Geophys. Res.*, *113*, D13204, doi:10.1029/2007JD008782.

Zhang, K. M., and A. S. Wexler (2002), Modeling the number distributions of urban and regional aerosols: Theoretical foundations, *Atmos. Environ.*, *36*, 1863–1874.

───────────────

R. C. Easter and R. A. Zaveri, Atmospheric Science and Global Change Division, Pacific Northwest National Laboratory, MSIN K9-30, P.O. Box 999, Richland, WA 99352, USA. (richard.easter@pnl.gov; rahul.zaveri@pnl.gov)

N. Riemer, Department of Atmospheric Science, University of Illinois at Urbana-Champaign, 105 South Gregory Street, Urbana, IL 61801, USA. (nriemer@illinois.edu)

M. West, Department of Mechanical Science and Engineering, University of Illinois at Urbana-Champaign, 1206 West Green Street, Urbana, IL 61801, USA. (mwest@illinois.edu)